A "principal stress cap" model for stresses in a circular silo with an off-centre core: finite core models, including filled silos, incipient flow and switch stresses

Matchett, A. J.; Langston, P. A.; McGlinchey, D.

Published in:
Chemical Engineering Research and Design

DOI:
10.1016/j.cherd.2015.12.010

Publication date:
2016

Document Version
Author accepted manuscript

A "principal stress cap" model for stresses in a circular silo with an off-centre circular core: finite core models, including filled silos, incipient flow and switch stresses

A.J.Matchett, University of Teesside(retired) ; P.A..Langston, Faculty of Engineering, University of Nottingham; D.McGlinchey, School of Engineering, Glasgow Caledonian University

Keywords: bulk solids; eccentric silo; yield; stresses

Abstract

Stresses have been modelled in a silo with offset centre of stress and finite circular core, using the methodology developed in Matchett, Langston and McGlinchey, CHERD(2015), vol 93, 330-348. Several types of core-annulus stress interactions have been proposed and some of the problems in the original Virtual Core model have been ameliorated. However, the selection of the most appropriate model is limited by lack of data on internal stress distributions within silos and the observation that different internal structures can give similar wall stress values.

Passive systems with convex stress cap and active stress systems with concave stress cap have been modelled. In order to keep wall shear stresses and internal stresses below the yield limits, the model suggests that deep, completely-filled silos would have very small values of wall arc normal angles, β_c and β_w and stress eccentricity, Ecc. Deep, filled silos with high stress eccentricity and large wall normal angles are not viable.

Incipient flow and the stress switch have been simulated. Output data suggest wide variation in wall stresses both axially and azimuthally are possible, at high stress eccentricities, which would have structural implications.

Contact:

Prof A.J.Matchett(retired), 15 Rufford Close, Guisborough, Redcar & Cleveland TS14 7PU, England
44-1287 637262
matchett15@ntlworld.com

Introduction

Matchett, Langston and McGlinchey(2015) developed a three-dimensional model of asymmetrical stresses in a cylindrical silo and the present paper is a continuation of the work presented there.

Silos with eccentric discharge have long been known to give problems of flow and structural integrity, due to variations in wall stresses both vertically and azimuthally: Sadowski and Rotter(2011); bulk-online forum(2015). Workers take encouragement from Carson's assertion (Carson, 2000) that stress and flow eccentricity is one of the major causes of silo failure.
There is an extensive body of literature in this field and several excellent reviews: for example Sielamovic et al(2010).
Since the previous paper, studies of eccentricity have continued to be published:
Recent publications in this field can be divided into 3 broad, often overlapping categories:

Structural analysis, including vessel stresses, failure and buckling.
Experimental studies: these may be model-based or studies of full-scale silos.
Modelling: the use of DEM, FEM and continuum models to predict bulk behaviour.

Investigations may include stresses generated, flow patterns and/or both. It is generally accepted that flow patterns affect stresses during discharge - Sielamovicz et al(2010)

Structural analysis: there continues to be a lively interest in vessel structures. Buckling has been analysed in silos of different methods of construction - Wojcik and Tejchman(2015), Sondej et al(2015). Sondej et al considered the implications of their work on the design codes.

Experimental studies: Sielamovicz et al(2015) continued their studies of eccentric flow patterns in a "2-d" model silo, following on from Sielamovicz et al (2010, 2011). On a much larger scale, Ramirez-Gomez et al(2015) measured stresses in the roof sections of an agricultural silo.

Modelling: Wang et al(2015) used their FEM system to analyse a flat-bottomed silo, predicting stresses, including a comparison with experimental data. Wojcik and Tejchman(2015) used a hypoplastic constitutive model within a FEM algorithm for sand to generate bulk solids stresses in their work on buckling, illustrating the fluidity of categories above. Wang et al(2015) used a macroscopic elasto-plastic constitutive model with linear Drucker-Prager criterion and a perfect plastic flow rule.
The authors' own paper (Matchett et al, 2015) is discussed below.

It is useful to differentiate between eccentric systems in which the core or flow channel touches the silo wall, and those systems in which the core/flow channel is eccentric but does not touch the wall. Several analyses model systems with core touching the wall: Sadowski and Rotter(2010), Sielemovic(2010, 2011, 2015). Eurocode 1(2006) is based upon this approach. The model of Matchett et al(2015) uses a core that does not touch the wall. The geometrical complexities make this an issue for further development.

Matchett, Langston and McGlinchey(2015) developed a three-dimensional model of asymmetrical stresses in a cylindrical silo with an inner, offset, circular core - see Figure 1. The model was based upon the principal stress cap concept of Enstad(1975). The reader is referred to the original paper for details of the model.: Matchett, Langston and McGlinchey(2015)

The output from the model was compared to wall stress data from a DEM simulation for a completely filled silo(r_1=0), with reasonable agreement. There were problems at X=0, (R_1=0) leading to a discontinuity in σ_3 and excessive stress peak values around ε_1=0 in deep beds with high eccentricity(Ecc). The hypothesis of a virtual core was proposed, but this was not entirely satisfactory. It was suggested that this problem might be overcome by use of an actual, finite core, rather than the virtual core.

The present paper extends the work of the first paper to include real, finite cores. It will model the following systems:

i) Systems with static, finite cores(r_1>0) and their properties
ii) Two core-annulus stress interactions will be considered: σ_1-continuity; and the Common Interfacial Plane - CIP
iii) Convex stress caps with passive stress state - the usual implementation of the Enstad principal stress cap method
iv) Concave stress caps with active stress states
v) Systems of incipient coreflow
vi) Switch stresses

Simulations will be conducted on a hypothetical bulk solids material with properties shown in Table 1:

Table 1 properties of test bulk material for use in simulations

Property	Symbol	Units	Formula	Value
Bulk density	ρ	Kg/m^3		1500
Angle of internal friction	ϕ	Degrees (radians)		30
Coefficient of wall friction	μ_w	-		0.25
Angle of wall friction	ϕ_w	Degrees (radians)	$\phi_w = \arctan(\mu_w)$	16.7
Minimum wall normal angle, β_w, active		Degrees (radians)	$0.5\left(\arcsin\left(\frac{\sin\phi}{\sin\phi_w}\right) - \mu_w\right)$	9.2
Maximum wall normal angle, β_w, passive		Degrees (radians)	$0.5\left(\arcsin\left(\frac{\sin\phi}{\sin\phi_w}\right) + \mu_w\right)$	25.9
Angle of shear plane in bulk material at yield minimum			$\frac{\pi}{4} - \frac{\phi}{2}$	30
Angle of shear plane in bulk material at yield maximum			$\frac{\pi}{4} + \frac{\phi}{2}$	60
Ratio of principal stresses at yield - active	$\mathbf{J_{active}}$		$\frac{1-\sin\phi}{1+\sin\phi}$	0.3333
Ratio of principal stresses at yield - passive	$\mathbf{J_{passive}}$		$\frac{1+\sin\phi}{1-\sin\phi}$	3
M - a measure of shear to compressive stress ratio	**M**			1

The principal stress cap model for eccentric stresses in a silo (Matchett et al, 2015)

The essential features of the geometry of the model are:

A circular silo of radius r_2 contains an inner core of radius r_1 offset from the centre of the outer silo by distance h - a plan view is shown in the top section of Figure 1.

Eccentricity, Ecc, is defined as:

$$Ecc = \frac{h}{r_2 - r_1} \qquad (1)$$

The model is based upon a co-ordinate system (ε_1, X, Z):

ε_1 is the angle of rotation of point P(ε_1, X, Z) about the centre of circle X projected onto the horizontal plane and is a measure of azimuthal rotation.

X is the x co-ordinate of the azimuthal principal stress path projected onto the horizontal plane as a circle of radius R_1, where the circle cuts the x-axis. In 3-d space the stress path is elliptical. The circle X also represents a constant arc angle, ε_2: the angle between the line of action of principal stress σ_3 and the vertical plane. ε_2 varies from β_c at the annulus core to β_w at the silo wall.

ε_3 is the slope of the plane along which σ_2 acts, as seen from the direction of ε_1.

Z is the z co-ordinate of the principal stress cap at the inner core

At point P(ε_1, X, Z), a set of local Cartesian co-ordinates (x_1, x_2, x_3) coincide with directions of principal stresses σ_1, σ_2, σ_3. A typical principal stress surface is shown in the lower section of Figure 1 with local axes and principal stresses at point P marked.

σ_1 acts towards the outer wall (along the ψ_1-line, Matchett et al(2015))

σ_2 acts azimuthally along the elliptical stress path in 3-d space which projects horizontally as the X-line

σ_3 acts normally to the principal stress cap surface(along the ψ_2-line, Matchett et al(2015))

Three partial differential equations in the principal stresses were than determined from force balances:

$$\frac{\partial}{\partial \varepsilon_1}\left[\sigma_2 R_2 \frac{\partial \varepsilon_2}{\partial X}\frac{\partial w_2}{\partial Z}\right] = -\sigma_1 \frac{R_1}{\cos\varepsilon_3}\frac{\partial w_2}{\partial Z} E \frac{\partial \psi_1}{\partial X} - \sigma_3\left(\frac{R_1}{\cos\varepsilon_3}\right) R_2 \frac{\partial \varepsilon_2}{\partial X}\frac{D\varepsilon_3}{DZ} + \rho g R_1 R_2 \frac{\partial \varepsilon_2}{\partial X}\frac{\partial w_2}{Z}\cos\varepsilon_2 \tan\varepsilon_3 \quad (2)$$

$$\frac{D}{DX}\left[\sigma_1 \cos\varepsilon_2\right] = -\frac{\sigma_1}{R_1\cos\varepsilon_3}\left(\frac{\partial w_1}{\partial X}\right)\left(\frac{\partial w_2}{\partial Z}\right) + \sigma_2\left(\frac{R_2}{R_1}\right) E \frac{\partial \varepsilon_2}{\partial X}\frac{\partial w_2}{\partial Z} - \sigma_3\left(\frac{R_2}{\cos\varepsilon_3}\right)\frac{\partial \varepsilon_2}{\partial X}\frac{D\varepsilon_2}{DZ} + \rho g R_2 \frac{\partial \varepsilon_2}{\partial X}\frac{\partial w_2}{\partial Z}\sin\varepsilon_2$$

or

$$\frac{\partial}{\partial X}\left[\sigma_1 \cos\varepsilon_2\right] = -\frac{\partial}{\partial \varepsilon_1}\left[\sigma_1 \cos\varepsilon_2\right]\frac{\partial \psi_1}{\partial X} - \frac{\sigma_1}{R_1\cos\varepsilon_3}\left(\frac{\partial w_1}{\partial X}\right)\left(\frac{\partial w_2}{\partial Z}\right) + \sigma_2\left(\frac{R_2}{R_1}\right) E \frac{\partial \varepsilon_2}{\partial X}\frac{\partial w_2}{\partial Z} - \sigma_3\left(\frac{R_2}{\cos\varepsilon_3}\right)\frac{\partial \varepsilon_2}{\partial X}\frac{D\varepsilon_2}{DZ} + \rho g R_2 \frac{\partial \varepsilon_2}{\partial X}\frac{\partial w_2}{\partial Z}\sin\varepsilon_2 \quad (3)$$

$$\frac{D}{DZ}\left[\frac{\sigma_3}{\cos\varepsilon_3}\right]=-\left[\frac{\sigma_3}{\cos\varepsilon_3}\right]\left(\frac{1}{R_2}\frac{\partial w_2}{\partial Z}+\frac{W}{R_1}\right)+\left(\frac{\sigma_1}{R_2\cos\varepsilon_3}\right)\frac{\partial w_2}{\partial Z}+\left(\frac{\sigma_2}{R_1}\right)\frac{\partial w_2}{\partial Z}\frac{\partial \varepsilon_3}{\partial \varepsilon_1}-\rho g\frac{\partial w_2}{\partial Z}\cos\varepsilon_2$$

or

$$\frac{\partial}{\partial Z}\left[\frac{\sigma_3}{\cos\varepsilon_3}\right]=-\frac{\partial}{\partial \varepsilon_1}\left[\frac{\sigma_3}{\cos\varepsilon_3}\right]\frac{\partial \psi_1}{\partial X}\frac{DX}{DZ}-\frac{\partial}{\partial X}\left[\frac{\sigma_3}{\cos\varepsilon_3}\right]\frac{DX}{DZ}-\left[\frac{\sigma_3}{\cos\varepsilon_3}\right]\left(\frac{1}{R_2}\frac{\partial w_2}{\partial Z}+\frac{W}{R_1}\right)$$
$$+\left(\frac{\sigma_1}{R_2\cos\varepsilon_3}\right)\frac{\partial w_2}{\partial Z}+\left(\frac{\sigma_2}{R_1}\right)\frac{\partial w_2}{\partial Z}\frac{\partial \varepsilon_3}{\partial \varepsilon_1}-\rho g\frac{\partial w_2}{\partial Z}\cos\varepsilon_2$$

(4)

These were integrated numerically.

The reader is again referred to the previous paper for details, Matchett et al(2015)

Positive features of the model include:

- The model is based upon rigorous, true 3-dimensional forces balances in orthogonal, curvilinear co-ordinates, subject to the assumption of a smooth principal stress cap.
- It works in principal stress space, which eliminates the need to account for shear stresses.
- The resultant numerical algorithms are relatively simple to implement, and outputs are easy to understand and visualise.
- Solutions can be obtained and analysed quickly, with a run taking about 5-10 minutes
- The model is a direct extension of previous work by Janssen and Enstad

The limitations are:

- The bulk material is assumed to be a rigid-plastic solid.
- It is steady state and cannot predict inertial effects or model motion.
- The model cannot predict contraction/dilation effects.
- The principle stress cap geometry cannot be easily determined, except at limiting conditions. It must be assumed "a priori".
- Only the region of fully developed principal stress can be modelled, between the surcharge at the top of the silo and the silo base(Matchett et al, 2015)

The lack of physical data for internal stresses makes the setting of boundary conditions very challenging. This is particularly so for the "forgotten stress": azimuthal stress σ_2.

In the previous paper, the x-axis(ε_1=0) was used as the spine of the solution. Whilst little is known of σ_2, it is possible to infer σ_1 values and their derivatives at core and wall. These values were used to interpolate intermediate values of σ_1 between the core and the wall(X_{min}

to X_{max}) along the line at ε_1=0. The differential equation for σ_1(equation 3) was then transposed to find values of σ_2 along the spine. These values formed boundary conditions for subsequent integration of the equation in σ_2(equation 2).

Conditions at the wall(subscript w) were fixed to give a Janssenian response(Janssen, 1895) in a symmetrical silo(Ecc=0, equation 1):

$$\begin{aligned} X = X_{\max} &: \sigma_1 = \sigma_{1w} = K_w \sigma_{3w} && (a) \\ X = X_{\max} &: \frac{\partial \sigma_3}{\partial X} = \gamma_1 \sigma_{3w} && (b) \\ X = X_{\max} &: \frac{\partial \sigma_1}{\partial X} = \gamma_2 \sigma_{1w} = \gamma_2 K_w \sigma_{3w} && (c) \end{aligned} \tag{5}$$

These conditions were used along the spine, even in asymmetrical silos. Conditions along the spine are similar to those of a symmetrical silo in that ε_3=0 and it is a line of symmetry.

Equations 5 represent a logical and successful attempt(Matchett et al, 2015) to reconcile experimental observation, existing theory and the present model. However, there was possibly an excess of fitted constants, as γ_1 and γ_2 were considered to be independent parameters in the original paper(Matchett et al, 2015). They are problematic: they may be material properties; particle shape dependent; silo wall properties; wall -particle interactions or even an artifact of the model itself. Their values have been previously fixed empirically.

A simple model is proposed to eliminate one of these constants.

Consider volumetric strain at the wall - $\delta\upsilon_w$

$$\delta \upsilon_w = \delta e_{1w} + \delta e_{2w} + \delta e_{3w} \tag{6}$$

where δe_{iw} is the strain in direction x_i at the wall.

If strain at the wall always consists of slip along the wall, it can be postulated that:

$$\delta \upsilon_w = 0 \tag{7}$$

Now, let strain increment be proportional to stress increment:

$$\delta \upsilon_w \propto \ \delta \sigma_{1w} + \delta \sigma_{2w} + \delta \sigma_{3w} = 0 \tag{8}$$

Dividing by δX and taking the limit, at the wall:

$$\frac{\partial \sigma_1}{\partial X} = -\frac{\partial \sigma_2}{\partial X} - \frac{\partial \sigma_3}{\partial X}$$

From equation 5(b) & (c)

$$\gamma_2 = -\frac{\gamma_1}{K_w} - \frac{1}{\sigma_{1w}} \frac{\partial \sigma_2}{\partial X}$$

If the system at the wall is considered as a plane stress system in the 1-3 plane, then azimuthal strains may be considered negligible along the line $\varepsilon_1=0$, which is a plane of symmetry:

$$\gamma_2 = -\frac{\gamma_1}{K_w} \tag{9}$$

Equation 9 will be used throughout this paper.

The equation is a simplification and other models might be proposed as further information becomes available, for example in a situation with contraction/dilation in the wall region, then equation 7 would not apply and would be modified to include $|\delta\upsilon_w| \rangle 0$.

The Enstad Core and σ_1 continuity

The core/annulus boundary is a vertical surface at $X=X_{min}$; $R_1=r_1$ - see Figure 2.

Annulus principal stress σ_1 has value σ_{1c} and makes angle β_c with the horizontal. Across the interface in the core, principal stress σ_1 has value σ_{1core} and makes angle β_{core} with the horizontal.

σ_{1c} is a boundary condition for σ_1 at the core/annulus interface, and is a key feature of σ_1-interpolation along the line $\varepsilon_1=0$ through the annulus, Matchett et al(2015).

It is necessary to reconcile the two stress systems. There are a number of approaches to modelling the stress interactions at the core-annulus boundary. Two methods will be considered in this paper.

In the first instance, a method termed σ_1 continuity will be used, in which the σ_1 plane is assumed to have continuity across the interface. This implies that:

$$\begin{aligned} \beta_{core} &= \beta_c \\ \sigma_{1core} &= \sigma_{1c} \end{aligned} \tag{10}$$

This can be applied to a plane core:

$$\beta_{core} = \beta_c = 0 \tag{11}$$

A value of $\beta_{core}>0$ results in an Enstad core (Enstad, 1975):

$$\beta_{core} = \beta_c : \beta_{core} > 0 \tag{12}$$

Stresses within the core can be found from a vertical force balance, dependent upon assumptions made about the core.

For a plane core:

$$\begin{aligned}
&\beta_{core} = 0 \\
&\frac{d\sigma_{3core}}{dZ} = -\rho g \\
&\sigma_{1core} = J_{core}\sigma_{3core} + (J_{core} - 1)T_{core}
\end{aligned} \tag{13}$$

An Enstad core can be modelled as:

$$\begin{aligned}
&\frac{d\sigma_{3core}}{dZ} = -\rho g + \left(\frac{2}{r_1}\right)\sin(\beta_{core})\cos(\beta_{core})\sigma_{1core} \\
&\sigma_{1core} = J_{core}\sigma_{3core} + (J_{core} - 1)T_{core}
\end{aligned} \tag{14}$$

A system of boundary conditions along the line $\varepsilon_1=0$ can now be specified for the σ_1-interpolation method:

$$\begin{aligned}
&\varepsilon_1 = 0 : \\
&X = X_{\min} : R_1 = r_1 \; : \; \sigma_1 = \sigma_{1c} \\
&X = X_{\max} : R_1 = r_2 : \sigma_{1w} = K_w\sigma_{3w} : \frac{\partial\sigma_3}{\partial X} = \gamma_1\sigma_{3w} : \frac{\partial\sigma_1}{\partial X} = \gamma_2\sigma_{1w}
\end{aligned} \tag{15}$$

Equation 15 consists of 1 core and 3 wall boundary conditions. Other forms of boundary condition are possible along the x-axis, but there is clearly a danger of over-specification of boundary conditions in this approach: more boundary conditions than the partial differential equations merit. Implicit in over-specification is the tendency to impart whatever properties are desired, into the equations.

Equations 13 and 14 assume uniformity of stress across the core, but more sophisticated models would be possible.

Core-annulus interactions: The Common Interfacial Plane (CIP)

The second model of interaction considered in this paper is one in which the common plane is not coincident with the planes of principal stress or the core wall. This has been termed the Common Interfacial Plane method, or CIP method.

Assume that the σ_1-σ_3 stress system may be treated as a plane stress system, and the stresses may be analysed by Mohr circles. The normal to this plane is a horizontal, circle and is the line if action of principal stress σ_2.

The common plane of the two systems is at angle θ_1 to σ_{1c} and θ_2 to σ_{1core} - see Figure 2. This is represented on a Mohr circle diagram in Figure 3. This is for a case of passive stress in the

core and active stress at the annulus wall. Usually, σ_{1core} and σ_{3core} are know, as is σ_{3c}- equations 13 & 14. The aim is to find σ_{1c} and θ_1, by the method shown below. Equivalent equations for other states of stress in the core and at the annulus can easily be derived.

σ_{1c} acts as a boundary condition in the σ_1-interpolation method, as shown in equation 15

The common plane has shear stress τ_c and normal stress σ_c - see Figure 3

From Figure 3:

$$\theta_2 = \theta_1 + \beta_{core} - \beta_c$$
$$\bar{\theta}_2 = \pi/2 - \theta_2 \qquad (16)$$

and

$$p_{core} = (\sigma_{1core} + \sigma_{3core})/2$$
$$q_{core} = (\sigma_{1core} - \sigma_{3core})/2$$
$$p_c = (\sigma_{1c} + \sigma_{3c})/2$$
$$qc = (\sigma_{3c} - \sigma_{1c})/2$$
$$\tau_c = q_c \sin(2\bar{\theta}_2) = q_{core} \sin(2\theta_1) \qquad (17)$$
$$\sigma_c = p_c + q_c \cos(2\bar{\theta}_2) = p_{core} + q_{core} \cos(2\theta_1) \qquad (18)$$

Equations 17 and 18 can be solved numerically, using a number of approaches. We used substitution followed by successive approximation, with constraints to limit the solution for θ_1 within the range 0-π and that σ_{1c} lies in the appropriate range of values, in this case, σ_{1c} should lie between σ_{1core} and σ_{3core}.

The CIP approach allows a discontinuity between the core and the annulus, in both stresses and stress directions.

Comparisons of Internal Principal Stress Structures

Our original paper modelled a completely filled silo section with an off-centre centre-of-stress. The boundary conditions imposed produced a Janssen-like wall normal stress response (Matchett et al, 2015). However, there were problems with the internal stress distributions around the centre-of-stress. Whilst the boundary conditions imposed continuity in σ_1 and σ_2 at the centre-of-stress, there were problems with "vertical" stress σ_3: the values of σ_3 were not constant at the centre-of-stress, but varied with azimuthal parameter ε_1, which is conceptually difficult for a core that has become a single point. There was a large, excessive peak in value

of σ_3, around ε_1=0, which increased with depth and eccentricity. The core was therefore referred to as a "Virtual Core". This is a name, rather than an explanation.

Table 2 Comparison of internal structure: Figures 4, 5 & 6

Bulk properties are given in Table 1

Key to notation:

VC : virtual core model(Matchett et al, 2015)

ECA : Enstad core, σ_1-continuity model; Active core

CIPA : Common Interfacial Plane model; Active core

ECP : Enstad core, σ_1-continuity model; Passive core

CIPP : Common Interfacial Plane model; Passive core

Parameter	VC	Plane Core	ECA	CIPA	ECP	CIPP
Common Parameters						
r_1 (m)	0.5					
r_2 (m)	2					
Z_{max} (m)	15					
h (m)	1					
β_w (degrees)	15^o					
K_w (-)	2					
γ_1 (m^{-1}	-1					
$N\varepsilon_1$	37					
N_X	51					
N_Z	1000					
Individual Values						
Ecc	0.5	0.667	0.667	0.667	0.667	0.667
β_c	-	0	7.436	7.436	7.436	7.436
β_{core}	0	0	7.436	0	7.436	0
J_{core}	-	0.333	0.333	0.333	3	3
T_{core}	0	0	0	0	0	0

It was suggested that a finite core may alleviate, or remove the peaks in σ_3 around the core (Matchett et al, 2015). Therefore, a system has been modelled with a finite core, with conditions shown in Table 2, using the σ_1-continuity and CIP models of core-annulus interaction described above - equations 10-18.

The outputs of the models have been plotted as wall normal stress versus Cartesian value z, in Figures 4a & 4b. Figure 4a compares models with an active core: Virtual Core versus σ_1-

continuity versus CIP. Figure 4b compares active and passive cores for the σ_1-continuity and CIP models.

The wall normal stress responses are all Janssenian. Furthermore, the nature of internal stress model does have an effect on wall normal stress, however, with the exception of the CIP passive simulation at $\varepsilon_1=0$, differences are relatively small, with a range of $5.4*10^4$-$7*10^4$ Pa. The responses are not significantly different such that the internal stress pattern could be deduced simply from the wall normal stress data.

The effects of the core model upon internal stress are shown in Figures 5a and 5b, where Figure 5a shows the variation in principal stress σ_3 along the line at $\varepsilon_1=0$ (positive x-axis), and Figure 5b shows the variation along the line at $\varepsilon_1=180^o$ (along the x-axis for negative values of x).

The peak in σ_3 in the Virtual Core model can be seen disappearing vertically off the graph in Figure 5a. The Plane Core model has moved the peak to the edge of the core. It has a higher magnitude than the Virtual Core model.

The σ_1-continuity and CIP have greatly reduced the peak magnitude along the $\varepsilon_1=0$ line, but there remains a discontinuity in σ_3 at the core wall.

Figure 5b shows the discontinuity in σ_3 at $\varepsilon_1=180^o$.

Therefore, the σ_1-continuity and CIP models have brought peaks in σ_3 down to reasonable values, but the discontinuities remain.

The σ_1-continuity model preserves continuity in σ_1, as the name suggests, but has discontinuity in σ_2 and σ_3. The CIP model gives discontinuity in all 3 principal stresses at the core.

Principal stress discontinuities would be acceptable in situations where the core was expected to be a different stress regime to the rest of the silo: incipient coreflow and coreflow. However, for a settled, filled silo, it would be difficult to argue why there should be discontinuity at any particular point, unless there were a history or some other justification.

Two other effects of structure upon stress are shown in Figures 6 & 7. Figure 6 shows the effects of core radius r_1, and Figure 7 shows the effects of eccentricity (Ecc) upon wall normal stress.

As core radius (r_1) and eccentricity (Ecc) increase, the wall normal stress decreases, as shown by the stress at a depth of 10m. There is also a tendency for azimuthal variation to increase with an increase in r_1.

If a set of experimental wall normal stress data were given for a filled silo, a model could be made to fit that data by changing r_1 or Ecc, or both. Again, it is impossible to relate wall normal stress data uniquely to an internal principal stress structure within the silo.

The reverse stress cap and active stress

The traditional picture of the stress state in the silo part of a storage vessel, is one of near-vertically aligned principal stress paths, converging on the centre-line of the silo, see Fayed and Otten, 1997, page 409 and Figure 8a. This is associated with an active state of stress in the silo section of the hopper. The near-vertical stress lines are equivalent to σ_3 in our model - equations 2, 3 & 4. Such a situation would be equivalent to a concave surface of the principal stress cap - Figure 8b.

Principal stress data for such a simulation are shown in Figure 9. Wall stresses are given in Figure 10.

Clearly, the principal stress cap model is able to describe active, concave stress cap systems, as well as the convex, passive systems more usually modelled, Enstad(1975). The radii R_2 are negative, hence the concave, rather than convex principal stress surface. Furthermore, in order to get a Janssenian wall normal stress response, it is necessary that the stress field be active, in particular $K_w<1$.

The converse applies to the passive, convex system in which $K_w>1$ for a Janssenian response.

As far as the authors are aware, this is the first time that an active, concave principal stress cap system has been explicitly modelled.

Yield and friction criteria

The core stress parameters J_{core} and T_{core}, plus the wall principal stress ratio K_w impose principal stress ratios at the boundaries of the system. However, the parameter K_w only operates at the wall at $\varepsilon_1=0$, as part of the σ_1 interpolation procedure - Figure 5. Throughout the rest of the material in the silo, there are no restrictions to stress ratios: stresses are determined purely by the force balances - equations 2-4. Therefore, stresses may exceed frictional and yield limits, because of the lack of constraint within the model, and it is necessary to test the outputs against yield criteria.

Three types of test will be presented in the following section:

i) principal stresses in tension

ii) Wall Yield Function - WYF

iii) Conical Yield Function - CYF

i) Principal Stresses in Tension

Non-cohesive materials cannot support principal stresses in tension. Even for cohesive materials, the tensile strength of a bulk solid is relatively small, and so principal stresses in tension cannot exceed to tensile strength. Hence for principal stress σ_i (i=1, 2, 3)

$$\sigma_i \geq -T_{core} \qquad (19)$$

Therefore, any simulation that produces excessive negative stresses in any of the principal stresses can be rejected as non-viable. The material would deform, even if the stress state could come to exist in the first place.

The mechanics of this test will be demonstrated with reference to two of the simulations in Figure 4b: Common Interfacial Plane, active core (CIPA); and Common Interfacial Plane, passive core (CIPP).

Apart from ε_1=0 for CIPP, the wall stress data are very similar. The principal stress distributions across a principal stress cap can be extracted from the data, and data for σ_2 at depth (Z_o-Z)=15m are shown in Figure 11: CIPA(active core) in Figure 11a and CIPP(passive core) in Figure 11b. There are clearly large areas of the stress cap for the passive core that are negative (in tension) and hence non-viable.

The difference in internal principal stress structure(active or passive) could not be deduced from the wall friction data - Figure 4b, although CIPP at ε_1=0 is an outlyer. Furthermore, an apparently benign wall stress distribution prediction (CIPP) can hide an unfortunate internal structure.

ii) Wall Yield Function - WYF

Wall shear stresses vary azimuthally and with depth - Figures 10a-c, for example. If an appropriate ratio of shear stress to normal stress exceeds limiting wall friction, then the material will deform and slide along the wall. Hence, the stress structure is not sustainable. A wall friction test will be proposed, as follows:

In order to transpose from original axis system (x, y, z) to a system aligned with the direction of principal stresses (x_1, y_1, z_1) the following rotations of axes must be made, in the order stated below - see Figure 1:

1. Rotate anticlockwise by angle ε_1 about the z-axis (axis 3)
2. Rotate clockwise by angle $-\varepsilon_3$ about the x-axis (axis 1)
3. Rotate anticlockwise by angle ε_2 about the y-axis (axis 2)

Therefore, in order to find the shear stresses aligned with the wall, one must rotate the wall principal stresses by angle ($-\varepsilon_2$) about the x_2 axis, using rotation matrix $R_{(-\varepsilon_2)}$:

$$R_{-\varepsilon_2} = \begin{pmatrix} \cos\varepsilon_2 & 0 & \sin\varepsilon_2 \\ 0 & 1 & 0 \\ -\sin\varepsilon_2 & 0 & \cos\varepsilon_2 \end{pmatrix} \quad (20)$$

This gives the following stresses in the plane of the wall:

- σ_{11} - wall normal stress
- σ_{12} - wall shear stress in the lambda plane at angle ε_3 to the horizontal. This has a value of zero, as this direction is the line of action of principal stress σ_2
- σ_{13} - shear stress normal to the lambda plane at angle ε_3 to the vertical.

Using these values, the Wall Yield Function, WYF, can be defined for a non-cohesive material:

$$WYF = \left|\frac{\sigma_{13}}{\sigma_{11}}\right| - \mu_w \quad (21)$$

When the WYF is less than zero, then the forces are less than limiting friction and the system is sustainable.

The wall stresses used in the calculation of WYF are such that the direction of σ_2 is normal to the plane of the wall stresses - it is aligned along direction ε_3. Other directions could be used, for example vertical shear stress and wall normal stress. Thus, WYF is an indicator rather than an absolute measure.

WYF>=0 then the forces exceed or equal the wall friction limit and the system is non-viable: wall slip will take place, affecting the principal stress orientation and hence negating the simulation.

The WYF was applied to the Enstad core, active model of Figure 4, Table 2 (ECA). The data are shown in Figure 12.

The WYF passes through a minimum before increasing steadily with depth, except for ε_1=0, which is controlled by the σ_1 interpolation process and has a fixed shear stress ratio, through constant K_w. The WYF exceeds zero at a depth between 7 and 9m and continues to increase. Therefore, the simulation ECA is not viable from a wall friction viewpoint below these depths.

The procedure for a valid simulation must be to change some of the parameters used in the original simulation to attempt to maintain WYF<0. This may be done by changing β_w, β_c and/or K_w.

Figure 13 shows a simulation with $\beta_w=7^o$ and $\beta_c=\beta_{core}=3.5^o$.

The shape of the WYF is similar to Figure 12, except that the value of WYF has been maintained below zero: in a viable situation.

Therefore, viability can be conferred upon a system by suitable selection of parameter values. In particular, simulations have shown that wall shear stress could be maintained at acceptable levels by:

- reducing the value of β_w and β_c;
- reducing the value of K_w;
- reducing eccentricity (Ecc)

iii) Yield Function: The Conical Yield Function CYF

There are many version of the yield function: Tresca; von Mises; Mohr-Coulomb and several others (Nedderman, 1992). They differentiate between a state of stress within the yield locus, and those on the boundary or outside the yield locus.

The model gives principal stresses throughout the silo, and so it is possible to calculate any number of yield functions. The example of the Conical Yield Function, CYF, will be the example shown in this paper. Nedderman, (1992) defines the Conical Yield Function as:

$$
\begin{aligned}
&CYF = (\sigma_1 - \sigma_2)^2 + (\sigma_2 - \sigma_3)^2 + (\sigma_3 - \sigma_1)^2 - 6M^2\bar{\sigma}^2 \\
&\bar{\sigma} = (\sigma_1 + \sigma_2 + \sigma_3)/3 \\
&or \\
&CYF = s_1^{\,2} + s_2^{\,2} + s_3^{\,3} - 2M^2\bar{\sigma}^2 \\
&s_i = (\sigma_i - \bar{\sigma}) \\
&CYF' = CYF/10^{10}
\end{aligned}
\qquad (22)
$$

As with the Wall Yield Function, when the CYF is less than zero, then the system is within the yield locus and is viable. When CYF>=0, the system is on the boundary or outside the yield locus and is non-viable. CYF' is the value of CYF divided by 10^{10}. This makes the numerical values more amenable.

Nedderman(1992) equates the value of M to sinϕ. This would make it equal to 0.5. Dependent upon the value and effect of the intermediate principal stress, then M could take a value of 0.5-1.2, using the parameters given in Table 1. Schofield and Wroth(1968) give M in the range 0.85-1 for Critical State Models. In this study a value of 1 will be taken for M. Larger or smaller values would move the CYF down or up respectively - Table 1.

Figure 13 shows that the conditions of simulation are acceptable from the viewpoint of the WYF. The same conditions are shown in Figure 14, where the CYF' is shown over the stress

cap at depth (Z_o-Z) of 15m, in X-ε_1 space. The CYF' exceeds zero in a region around the core for ε_1 in the range 50^o to 180^o. Clearly, even though WYF criteria have been met, CYF criteria have not been met over the whole of the principal stress cap at a depth of 15m.
Some of the information in Figure 14 can be condensed into a single parameter: the Principal Stress Cap Yield Quotient, or YQ:

YQ = the fraction of cells in a principal stress cap array in X-ε_1 space in which the CYF is greater than zero

(23)

Figure 15 shows YQ as a function of depth (Z_o-Z) for a number of simulations, demonstrating effects of eccentricity (Ecc) and wall normal angles. See Table 3 for details.

Table 3 Details of conditions for the simulations in Figure 15

Simulation	r_1 (m)	r_2 (m)	Ecc (-)	h (m)	β_w (deg)	$\beta_c=\beta_{core}$ (deg)	K_w	γ_1
Basecase Figs 13 & 14	0.5	2	0.667	1	7	3.5	2	-1
Basecase: Ecc varied	0.5	2	var	var	7	3.5	2	-1
Basecase: half angles	0.5	2	0.667	1	3.5	1.75	2	-1
Concave 1	0.5	2	0	0	-7	0	0.95	-1
Concave 2	0.5	2	0	0	-5	0	0.95	-1

Figure 15 shows that the YQ remains below zero until a critical depth (Z_o-Z) is reached. This critical depth decreases as eccentricity increases and as wall angle β_w increases. Once the critical depth is exceeded then the YQ increases steadily with depth.
Above a certain Eccentricity(see Ecc=0.8 in Figure 15), the system can never sustain a stress system within the yield locus for the conditions modelled here.
The preceding argument applies equally to concave yield surfaces - Figures 8, 9 & 10.

The analysis implies that deep beds in completely filled silos with fully developed stress systems cannot support high stress eccentricities or relatively large wall and core angles. This is supported by both the σ_1-continuity and CIP core annulus interaction algorithm outputs. The data from the Virtual Core model in the first paper (Matchett et al, 2015) can also be

interpreted to give the same conclusion: deep beds with high eccentricity and/or large wall normal angles give excessive stress peaks at the Virtual Core, which are not viable.

The magnitudes of the descriptors "deep" silo and "relatively large angles" can be quantified by the model.

Accepting the yield limitation criteria upon Ecc and β_w within a filled silo, the Virtual Core model (Matchett et al, 2015) may be the best approach. It removes the stress continuity problems at the core-annulus interface. However, these are replaced by the anomalies of the Virtual Core.

Incipient core-flow and the stress switch

Incipient core-flow will now be modelled. This is the stress situation at the core yield limit as the core is about to start to flow. It does not involve inertial terms or contraction/dilation effects. It is assumed that there is no immediate flow in the annulus.

There are several ways in which incipient flow may be modelled within this eccentric stress, silo simulation, and two will be considered here:

- σ_1 continuity at the core-annulus interface
- The use of the Common Interfacial Plane algorithm (CIP) at the interface

At incipient flow, it is generally accepted that the core, which is about to flow, will be in a state of passive stress with the arc normal angle equal its limiting passive value: 60^o in this case - Table 1.

The normal angle at the core ($\beta_c=\beta_{core}$) of 60^o is greater than the maximum wall normal angle of 25.9^o - Table 1. This enforces a concave principal stress surface system into the silo - Figures 8, 9 & 10, for the σ_1 continuity model. Therefore, K_w must be active and have a value less than 1. This approach implies yield or positive value of CYF at the core and the annulus wall.

The CIP model can allow β_{core} to be 60^o, whilst β_c and β_w may take other values, due to the discontinuity at the core-annulus interface.

Two simulations have been run to compare the two methods of modelling incipient flow. The conditions are shown in Table 4.

Wall normal and wall vertical shear stresses for the conditions in Table 4 are shown in Figures 16a & 16b respectively. The wall stresses are quite different, both quantitatively and qualitatively. In these circumstances, the choice of internal principal stress geometry has a great effect upon measured wall stresses.

Table 4 Conditions at incipient flow: see Figure 16

Parameter	σ_1 continuity model IF1	CIP model IF2
r_1 (m)	0.5	0.5
r_2 (m)	2	2
Ecc (-)	0.667	0.667
H (m)	1	1
β_{core} (deg)	60	60
β_c (deg)	60	3.5
β_w (deg)	10	7
K_w (-)	0.9	2
γ_1 (m^{-1})	-1	-1
YQ at depth (Z_o-Z)=10m	0.445	0.123

If conditions are changed at a specified depth during the simulation, then a version of the switch-stress calculation can be modelled (Nedderman, 1992, p166).

In this version, it will be assumed that the core is in an active stress state with σ_1 continuity at the core-annulus boundary above the switch. At the switch, the core stress state will be changed to passive $J=J_{passive}$, Table 1, with the core arc angle, β_{core} changed to the value at passive yield (60^o, Table 1). All parameters in the annulus remain unchanged, and it is assumed that the depth taken for the change in orientation of principal stresses in the core is negligible or does not greatly affect the outcome. This implies use of the CIP core-annulus interaction model below the switch. This is one of the simplest implementations of the switch stress, and other, more complex versions are possible.

It has been shown that deep silos can only support modest wall and core angles, and so values of 5^o and 2^o have been used. It is important to remain within the yield surface above the switch, but below the switch flow is imminent.

Figure 17 shows data for a switch stress scenario with a constant value of wall principal stress ratio K_w. Details are given in Table 5.

The responses of the principal stresses are shown in Figures 17a-c. σ_1 and σ_2 undergo a sudden dip at the switch, followed by a steady increase back to just above the pre-switch stress levels. σ_3 continues to increase steadily in the region of the dip. This translates into

wall normal stress responses, as shown in Figure 17d. There are azimuthal variations in stresses, which increase as eccentricity(Ecc) increases.

Table 5 Conditions for switch simulation in Figures 17 and 18

	Figure 17	Figure 18	Figure 19
Core radius r_1 (m)	0.5	0.5	0.5
Silo radius r_2 (m)	3.0	3.0	3
Eccentricity Ecc	0.75	0.75	0.95
Offset h (m)	2.25	2.25	2.375
β_w (deg)	5	5	5
β_c (deg) = β_{core} above switch	2	2	2
β_{core} (deg) below switch	60	60	60
γ_1	-1.5	-1.5	-2
Above switch			
J_{core}	0.5	0.5	0.333
T_{core}	0	0	0
K_w	2.1	2.1	1.1
Below switch			
J_{core}	2.5	2.5	3
T_{core}	0	0	0
K_w	2.1	2.5	3
Z_{max} (m)	30	30	30
Z_{switch} (m)	5	5	5

At the wall, at ε_1=0 and for all values of ε_1 at eccentricity, Ecc=0, then σ_1 is directly related to σ_3 through equation 5a. Thus, if the switch causes little variation in σ_3 - Figure 17c, then little change can be expected in σ_1, because of equation 5a.

It can be argued that as the state of stress changes at the core, during the switch, then an equivalent change might be expected at the wall, with an increase in K_w below the switch. This has been modelled in Figures 18, for conditions shown in Table 5, with an increase in K_w from 2.1 to 2.5 at the switch. The drop in stresses at the switch is no longer present, and the stress increases at switch are more pronounced in σ_1, σ_2 and wall normal stress. σ_3 increases gradually at the switch, as in Figure 17. However, the magnitude of the switch

stress can now be controlled by the programmer through the change in parameter K_w at switch. The magnitude of change could thus be calibrated by comparison with appropriate experimental data.

It is interesting to consider an extreme switch stress at conditions close to the maximum possible. Conditions are given in Table 5. the changes in J_{core} and K_w are the maximum possible. Wall normal stress variation with depth is shown in Figure 19 for a system with a high eccentricity: Ecc=0.95. Under these conditions, the switch can double wall normal stress (at ε_1=0). There are also large azimuthal normal stress variations.

Several other implementations of a switch stress are possible, including versions in which the annulus as well as core stress states change. Problems include:

- how the stress states change within the core and annulus
- how to model the transition from one stress state to the other

The implementation presented herein does give a methodology for quantifying the switch stress in eccentric stress systems, however imperfect.

Discussion

Overview: positive features -

This model is one of the few, perhaps very few dedicated models of eccentric stress in silos and hoppers. It is a true 3-dimensional model, based upon the principal stress cap approach of Enstad: Enstad(1975), Matchett et al(2015). The assumed model of principal stress geometry is such that it could be approximated to a wide range of shapes, provided that the principal stress surfaces are smooth and there are no discontinuities within the annulus.

The model can describe the perceived features of stress systems in a silo:

- Janssenian wall stresses: Figures 4 and Matchett et al(2015)
- Passive stress systems, Figures 4-7, Matchett et al(2015)
- Active stress state, Figures 8, 9 & 10
- Determination of yield conditions at the wall and internally and consideration of whether stress states remain within the yield surface, Figures 11-15
- Incipient coreflow - Figures 16
- Switch stresses - Figures 17, 18, 19

Overview: limitations and drawbacks-

This model probably represents the limit of the potential of the Enstad(1975) approach in its present form. It can only be applied to the region of fully developed stress between the surcharge and the base of the silo - Matchett et al(2015).

The model cannot predict the path of principal stress lines. Limiting values of these can be inferred from values of the controlling angles β_w, β_c and β_{core} - see Table 1.

From Mohr circle theory, for plane stress systems, the limiting values of wall normal angles, θ_{lim}, are:

$$\theta_{\text{lim}} = \frac{1}{2}\left\{\mu_w \pm \arcsin\left(\frac{\sin \mu_w}{\sin \phi}\right)\right\}$$

And limiting angles at the core-annulus interface, ζ_{lim}, is given by:

$$\zeta_{\text{lim}} = \frac{\pi}{4} \pm \frac{\phi}{2}$$

In a general case, angles can be stipulated within these limits, where principal stress geometry is assumed a priori and the resultant stress fields calculated. The data output must then be tested to determine whether the stresses remain within the yield surfaces.

The model is steady-state. It cannot model dynamic systems, where inertial terms are involved or systems with contraction/dilation. One simple reason for this, is that during a dynamic change and/or dilation, the principal stress lines would change orientation in some manner as yet unpredictable. Therefore, incipient flow is modelled, rather than flow, and dynamic effects are ignored in calculation of switch stress.

The model proposes an internal structure for the principal stresses within the silo, and from that, calculates the stresses throughout the silo. However, this is constrained by the lack of knowledge of stress fields within the silo, rather than limitations of the model, and two models of core-annulus stress interactions have been considered in the paper.

The simple fact that so many possibilities can be proposed illustrates the lack of information available to calibrate the model.

The model cannot predict stresses in systems where the core touches the silo wall, as in Eurocode 1(2006). Data indicate that stress variations can be much greater in such systems than predicted here - see Lapko(2010) for example. It remains to extend the present model to this situation.

Reconciling data from the model with other sources-

It was shown in our previous paper(Matchett et al, 2015) that the model can be fitted to wall stress data from a DEM simulation. Model parameters may be adjusted empirically to give a desired output. The reader is referred to the first paper(Matchett et al, 2015) for the data fitting methodology.

Unfortunately, such adjustment is almost purely empirical. It has been shown that a range of internal parameters can predict similar wall stresses, both in this paper and in the previous one: Matchett et al(2015).

More generally, silo stress data consist of wall stress measurements. The wall stress measurements consist mainly of wall normal stress. For a full survey see our previous paper, Matchett et al(2015). Wall normal stress is a key parameter in the structural design of a silo, as well as being the most widely measured of silo stress parameters and therefore features throughout this paper.

There are few examples, if any, of measured internal stresses in silos. Added to this, the authors do not know of any measurements of azumuthal stresses: σ_2 in this model. It is the "forgotten stress" in silo modelling. This makes comparisons difficult and boundary conditions cannot be easily formulated.

Wall stress data have been measured in a relatively large number of studies. Wall stress measurement is a poor indicator of the principal stress orientation within the centre of the silo. Wall stress measurements do not even give a definitive statement of principal stress orientation at the wall, as shown below:

Consider a general situation where wall normal stress, σ_c is measured in a plane stress system. This single measurement tells us the following about the principal stresses - see Figure 20, Mohr circle 1:

i) Minor principal stress $\sigma_{min}<=\sigma_c$

ii) Major principal stress $\sigma_{maj}>=\sigma_c$

This is clearly not an exact situation.

Some workers have also measured shear stress τ_c - Figure 20. Askegaard(1988) pioneered the use of embedded cells for this purpose, but papers presenting shear as well as normal data are few, compared to those measuring only normal stress. These two measurements now give a single point on the Mohr circle. But many Mohr circles could pass through that point: two such Mohr circles are shown in Figure 20: Mohr circle 1 and Mohr circle 2.

Thus, it would be possible for a model to predict the "right" wall stress, but get the underlying stress field quite wrong.

This inexact situation would be made much more complex in a 3-d situation with the third principal stress (σ_2) also participating. If wall stresses cannot pin down the stress situation at the wall, how can they be expected to extrapolate to predict stress distributions within the silo?

It has been shown that different internal stress structures can give similar wall stress values - for example, Figures 4. In a wider context, there are lots of different models, each of which can give reasonable agreement with wall stress data: FEM, DEM and continuum models. Within these categories, different authors use different approaches. For example within recent papers, Wojcik and Tejchman(2015) and Wang et al(2015) both use FEM but each uses a different constitutive model within their FEM framework. Likewise DEM models have used a range of particle contact interaction. Continuum models can also reproduce acceptable wall normal stresses.

These approaches cannot all be said to give a valid, overall description of stress and flow patterns in hoppers, but they all "work" to a greater or lesser extent.

Therefore:

When a model fits experimental wall stress measurements, this is a necessary, but not a sufficient condition for acceptance of the said model.

Without further corroborating evidence, the model may be considered as an empirical fit to the data with all the limitations that this implies.

Passive and active stress states within the silo-

The principal stress cap method has been used to model the passive, convex principal stress surfaces, typically seen in incipient flow in a hopper or silo section - Figure 16, where the major principal stress is equivalent to σ_1 in this model.

The model has also been used to describe active stress in the vertical-walled silo section, where the hypothesised, near-vertical lines correspond to σ_3 in our model and converge on the line of the centre of stress - Figures 8.

The model gives Janssenian wall stress responses in both cases, when the following rule applies:

- Passive stress state: convex principal stress cap: Kw>1
- Active stress state: concave principal stress cap(Figure 12b): Kw<1 (20)

Thus, the Kw value corresponds to the required stress state: $K_w>1$ = passive; $K_w<1$ = active.

If the above rule is not applied, in both cases, wall stresses increase exponentially.

As far as the authors are aware, this is one of the first attempts to explicitly model the active stress state, as shown in Figure 8.

Structural Implications-

The present model indicates large stress variations, both azimuthally and axially, associated with high stress eccentricity, measured by eccentricity(Ecc) - equation 1, and large wall normal angles β_w. Fortunately, in deep, filled silos, eccentricity and wall normal angle must remain modest, in order to maintain the stresses within the yield surfaces. However, if larger values were to occur, as a transient state, then there may be structural problems: for example the opening of an off-centre outlet with high eccentricity - Figure 19. Unfortunately, this model cannot describe transient situations and this must be taken into account in the interpretation of such data

Generally, there are large azimuthal variations in wall vertical shear stress, even at modest eccentricity and wall normal angles - for example, see Figure 16b. The resultant forces are limited by limiting friction, but even so, some regions of the wall circumference will be at limiting friction while others will be below this level. Wojcik and Tejchman(2015) state that buckling is caused by wall friction(rather than normal stress), particularly during eccentric discharge and therefore, the asymmetry of wall shear may be a critical factor.

Future Developments-

The implementation of the model is limited by lack of detailed information of the principal stress structure within a silo. There is a vital need for experimentation. Modern stress measurement technology should be capable of developing sensors that measure and transmit internal stresses from within a hopper/silo system.

Experimental work needs to be supported by simulation, using FEM and DEM. One possible approach would be to calibrate the model against internal properties taken from DEM and FEM simulations. Such an approach would be very labour-intensive.

This modelling approach is limited by the inability to calculate and predict principal stress lines related to the principal stress cap, rather than assuming them. It is not clear how this could be done efficiently within the context of the model. If it were possible, it may be feasible to model dynamic systems using the principal stress cap approach and incorporating changes in principal stress directions with motion.

Conclusions

Stresses have been modelled in a silo with a finite, off-centre core within the silo, using the principal stress cap approach.

Several types of core wall-annulus interaction are possible and two have been proposed in this paper. A finite, Enstad core with σ_1 continuity and an Enstad core, with the use of CIP Common Interfacial Plane interaction model greatly reduce the stress peak in σ_3, but discontinuity at the core remain to a greater or lesser extent (Matchett et al, 2015).

Passive, convex and active, concave principal stress systems can be described by this model.

Generally, it is not possible to predict internal principal stress structure from wall stress measurements.

The Wall Yield Function analyses and the Conical Yield Function (CYF) analyses suggest that wall normal angle, β_w, and eccentricity (Ecc) must be small in deep beds i.e. deep stable beds with high eccentricity and/or large wall normal angle are not viable.

Incipient coreflow and switch stresses have been modelled.

Implementation of the model is hindered by lack of information about the internal stress structures of materials in silos.

References

Askegaard V., J.Munch-Andersen, 1985. Results from tests with normal and shear cells in a medium-scale model silo,. Powder Technology, 44, 151-157

bulk-online forum, http://forum.bulk-online.com

Carson J.W., Silo Failures: case histories and lessons learned, Third Israeli Conference for Conveying and handling of Particulate Solids, Dead Sea, Israel, May 2000

Enstad G., 1975, On the theory of arching in mass flow hoppers, Chem.Eng.Sci. 30, 1273-1283

Eurocode 1, EN 1991-4, 2006. Action on structures - Part 4: Silos and Tanks. Brussels, Belgium.

Fayed M.E., L.Otten, Handbook of Powder Science and Technology, 2nd Edition, Chapman and Hall, New York, 1997

Janssen H.A., 1895. Versuche uber getreidedruck in silozellen, Zeitschrift verein Deutsche Inginieur, 39,1045-1049

Lapko A. 2010. Pressure of agricultural solids under eccentric discharging of cylindrical concrete silo bin. Int.Agrophysics 24, 51-56

Matchett A.J., P.A.Langston, D.McGlinchey. 2015. A model for stresses in a circular silo with an off-centre circular core, using the concept of a principal stress cap: Solutions for a completely filled silo and comparison with DEM data. Chemical Engineering Research and Design 93, 330-348

Nedderman R.M.(1992), Statics and Kinematics of Granular Materials, Cambridge University Press, Cambridge, England

Ramirez-Gomez A., E.Gallego, J.M.Fuentes, C. Gonzalez-Montellano, C.J.Porras-Prieto, F.Ayuga. 2015. Full-scale tests to measure stresses and vertical displacements in an 18.34m-diameter steel roof silo. 106, 56-65

Sadowski A.J., J.M.Rotter, 2011. Buckling of very slender metal silos under eccentric discharge. Engineering Structures, 33, 1187-1194

Schofield A., P.Wroth, 1968, Critical State Soil Mechanics, McGraw-Hill, New York, USA

Sielamovicz I., M.Czech, T.A Kowalewski. 2010. Empirical description of flow parameters in eccentric flow inside a silo model, Powder Technology 198, 381-394

Sielamovicz I., M.Czech, T.A Kowalewski. 2011. Empirical analysis of eccentric flow registered by teh DPIV technique inside a model silo, Powder Technology 212, 38-56

Sielamovicz I., M.Czech, T.A Kowalewski. 2015. Comparative analysis of empirical descriptions of eccentric flow in silo model by the linear and non-linear regressions, Powder Technology 270, 393-410

Sondej M., P.Iwicki, J.Tejchman, M.Wojcik. 2015. Critical assessment of Eurocode approach to stability of metal cylindrical silos with corrugated walls and vertical stiffeners. Thin-Walled Structures. 95, 335-346

Wojcik M., J.Tejchman. 2015. Simulation of buckling process of cylindrical metal silos with flat sheets containing bulk solids. Thin-Walled Structures. 932, 122-136

Yin Wang , Y.Lu, J.Y.Ooi. 2015. A numerical study of wall pressure and granular flow in a flat-bottomed silo. Powder Technology. 282, 43-54

Notation

SYMBOL	DESCRIPTION	UNITS
a_1	Relates projected circle radius R_1 to X $R_1 = a_1 X + a_1'$	-
a_1'	Constant relating R_1 to X – see a_1	m
a_2	Differential of projected circle centre $a_2 = \partial O_X / \partial X$	-
D	D/DX and D/DZ are differentials along the principal stress paths for changes in X & Z respectively	

e_1	Angle used in the calculation of R_2	rad
E	Factor relating rotation in the horizontal plane to rotation on the λ-plane	-
h	Inner circle offset	m
		-
k	Ratio of wall vertical to normal stress: Janssen model	-
K_w	Ratio of σ_1/σ_3 at the wall	-
M	Conical Yield Function parameter	-
r_1	Inner circle radius	m
r_2	Outer circle (silo) radius	m
R_1	Radius of projected horizontal circle of principal stress path	m
R_2	Radius of principal stress cap at a general point	m
R_{20}	Value of R_2 at $\varepsilon_1=0$	m
$R_{2\pi}$	Value of R_2 at $\varepsilon_1=\pi$	m
w_1	Arc length along ψ_1-line, seen as $\partial w_1 / \partial X$	m
w_2	Arc length along ψ_2-line, seen as $\partial w_2 / \partial Z$	m
x	x-axis co-ordinate	m
X	Intercept of projected horizontal surface with x-axis	m
X_o	Minimum value of X	m
X_{max}	Maximum value of X	m
x_1, x_2, x_3	Local Cartesian co-ordinates coincident with directions of principal stress	-
y	y-axis co-ordinate	m
z	z-axis co-ordinate	m
Z	Value of z for the inner radius of the principal stress cap	m
Z_o	Value of Z at the point of boundary conditions	m
β_c	Angle of circular arc to normal at inner core	rad
β_w	Angle of circular arc to normal at wall	rad
ε_1	Angle from x-axis in the horizontal plane	rad
ε_2	Angle from the vertical in the x-z plane at $\varepsilon_1=0$, rotated along the elliptical, principal stress path	rad
ε_3	Angle from the vertical – slope of the principal stress cap surface as seen from ε_1	rad
γ_1	Slope of principal stress, σ_3 at the wall	Pa/m
γ_2	Slope of principal stress, σ_1 at the wall	
ϕ	Angle of internal friction. A nominal value of 30^o has been used.	rad

λ	Characteristic slope of principal stress path ellipse when projected onto the x-z plane	rad
μ_w	Coefficient of wall friction. A nominal value of 0.3 has been used.	-
η	Surcharge friction factor	-
θ_{lim}	Limiting value of wall arc angle	rad
ζ_{lim}	Limiting value of plane of yield	rad
ψ_1	Angle of ψ_1-line to x-axis on the horizontal plane	rad
ψ_2	Angle of ψ_2-line to vertical – principal stress path for changes in Z	rad
ρ	Bulk density of the bulk solid in the silo	Kg/m^3
σ_1	Principal stress in x_1 direction	Pa
σ_2	Principal stress in x_2 direction	Pa
σ_3	Principal stress in x_3 direction	Pa

Figures

Figure 1 The principal stress cap and essential structure of the principal stress cap, eccentric silo model

Figure 2 Core-annulus interaction for the Common Interfacial Plane model - CIP model

Figure 3 Mohr circles for the Common Interfacial Plane model: Mohr circles of the core wall and annulus wall

Figure 4 Effects of internal structure on wall normal stress. Variation of wall normal stress with depth, as measured by z (Cartesian)
See Tables 1 & 2 for conditions
Figure 4a: different core models
Figure 4b: active and passive cores
VC **:** virtual core model(Matchett et al, 2015)
ECA **:** Enstad core, σ_1-continuity model; Active core
CIPA **:** Common Interfacial Plane model; Active core
ECP **:** Enstad core, σ_1-continuity model; Passive core
CIPP **:** Common Interfacial Plane model; Passive core

Figure 5 Internal stress distributions for different core models.
See Tables 1 & 2 for details
Figure 5a: σ_3 variation along the X-line at $\varepsilon_1=0^o$
Figure 5b: σ_3 variation along the X-line at $\varepsilon_1=180^o$
VC **:** virtual core model(Matchett et al, 2015)
ECA **:** Enstad core, σ_1-continuity model; Active core

CIPA : Common Interfacial Plane model; Active core

ECP : Enstad core, σ_1-continuity model; Passive core

CIPP : Common Interfacial Plane model; Passive core

Figure 6 Effects of core radius on wall normal stress: variation in wall normal stress with azimuthal variation ε_1, at depth (Z_o-Z) of 10m.
Conditions as in Table 2, except:
Active core, J_{core}=0.333; h=1 m throughout
Enstad core with σ_1-continuity.
$\beta_w=8^o$; $\beta_c=\beta_{core}=3^o$

Figure 7 Effects of Eccentricity (Ecc) on wall normal stress: variation in wall normal stress with azimuthal variation ε_1, at depth (Z_o-Z) of 10m.
Conditions as in Table 2, except:
Passive core, J_{core}=3; r_1=0.5 m throughout
Enstad core with σ_1-continuity.
$\beta_w=10^o$; $\beta_c=\beta_{core}=3^o$

Figure 8 Concave principal stress cap half-surface
r_1=0.5; r_2=2m; $\beta_c=\beta_{core}=-1^o$; $\beta_w=-10^o$
Figure 8a The accepted picture of lines of major principal stress in hopper/silo sections.
Figure 8b The shape of the principal stress cap surface

Figure 9 Principal stress surfaces in X-ε_1 space at depth (Z_o - Z) of 10m
Geometry as in Figure 8.
ρ=1500 kg/m^3; γ_1=-1; K_w=0.95; $\gamma_2=-\gamma_1/K_w$; Ecc=0.5
Figure 9a σ_1 in X-ε_1 space
Figure 9b σ_2 in X-ε_1 space
Figure 9c σ_3 in X-ε_1 space

Figure 10 Wall stresses for conditions in Figures 8 & 9
Figure 10a wall normal stress versus z
Figure 10b wall vertical shear stress versus z
Figure 10c wall horizontal shear stress

Figure 11 Principal stress σ_2 over the principal stress cap at depth (Z_o-Z)=15m.
The conditions are given in Table 2.
Figure 11a CIPA
Figure 11b CIPP

Figure 12 Wall Yield Function (WYF) as a function of ε_1 and depth for the simulation EPA in Figure 4. See Figure 2 for details

Figure 13 Wall Yield Function (WYF) as a function of ε_1 and depth for the simulation of revised conditions for the ECA simulation. Conditions as in Figure 4, Table 2 and Figure 12, except:
$\beta_w=7^o$; $\beta_c=\beta_{core}=3.5^o$

Figure 14 CYF' for the principal stress cap at depth (Z_o-Z) of 15m. Conditions as shown in Figure 13.

Figure 15 The Yield Quotient (YQ) for a range of simulations, including those in Figures 13 & 14. For details see Table 3.

Figure 16 Wall stresses for a silo at incipient core-flow. For conditions see Table 4
Figure 16a wall normal stress versus z
Figure 16b wall vertical shear stress versus z

Figure 17 Switch stresses in a silo section 3m radius and 30m tall: conditions shown in Table 5
Figure 17a Principal stress σ_1 versus Cartesian coordinate z
Figure 17b Principal stress σ_2 versus Cartesian coordinate z
Figure 17c Principal stress σ_3 versus Cartesian coordinate z
Figure 17d Wall normal stress in the region of the switch versus Cartesian coordinate z

Figure 18 Switch stresses in a silo section 3m radius and 30m tall with an increase in Kw below the switch: conditions shown in Table 5
Figure 18a Principal stress σ_1 versus Cartesian coordinate z
Figure 18b Principal stress σ_2 versus Cartesian coordinate z
Figure 18c Principal stress σ_3 versus Cartesian coordinate z
Figure 18d Wall normal stress in the region of the switch versus Cartesian coordinate z

Figure 19 Wall normal stress for conditions close to those of maximum magnitude switch stress. For conditions see Table 5
Figure 19a Overall wall normal stress variation with depth with ε_1 (deg) as a parameter
Figure 19b Wall normal stress in the region of the switch with ε_1 (deg) as a parameter

Figure 20 Wall stress measurements - the relation between wall stress measurement, Mohr Circles and their wider interpretation in terms of stress structure through the silo

Figure

Figure 1 The principal stress cap and essential structure of the principal stress cap, eccentric silo model

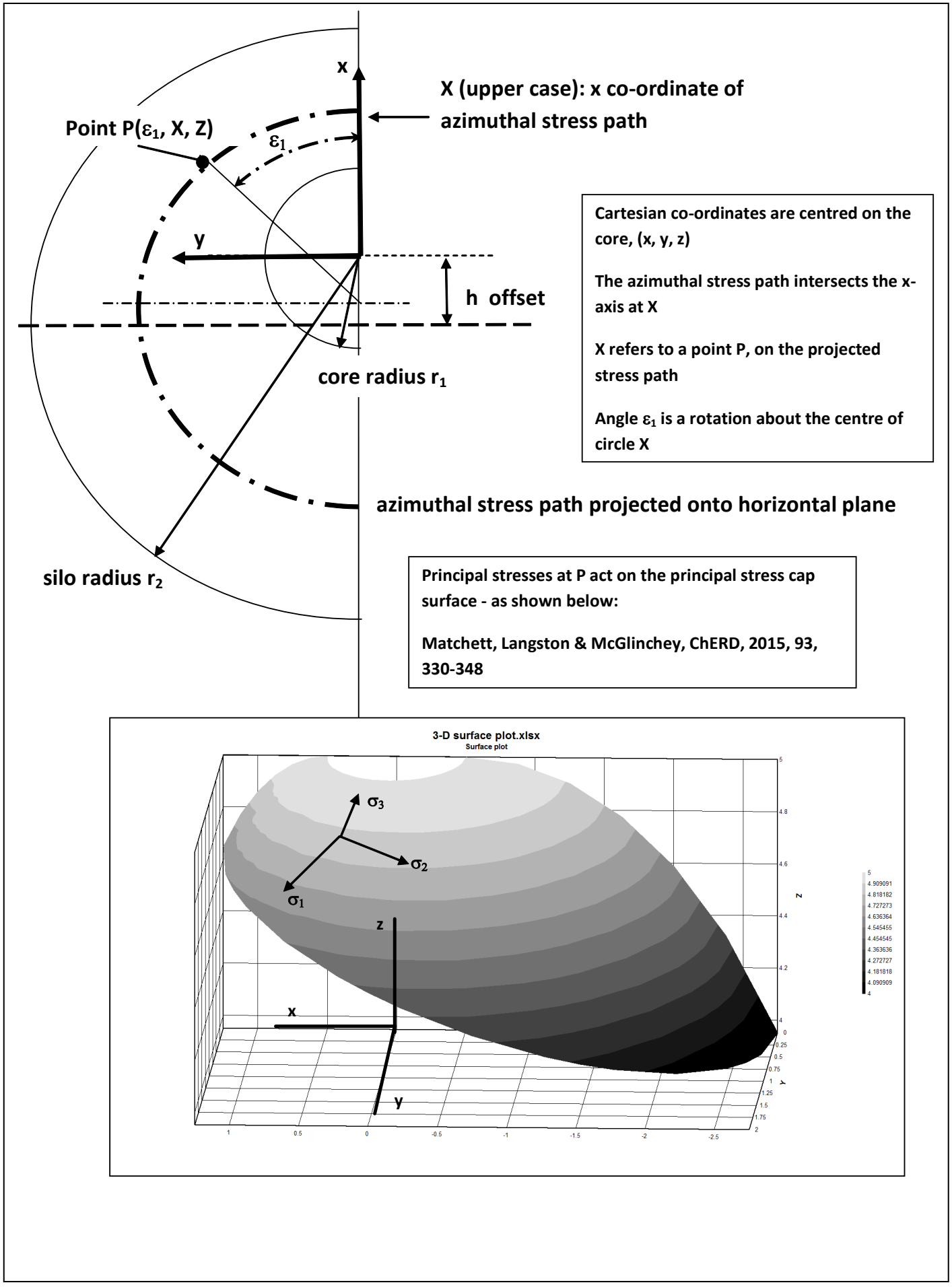

Figure 2 Core-annulus interaction for the Common Interfacial Plane model - CIP model

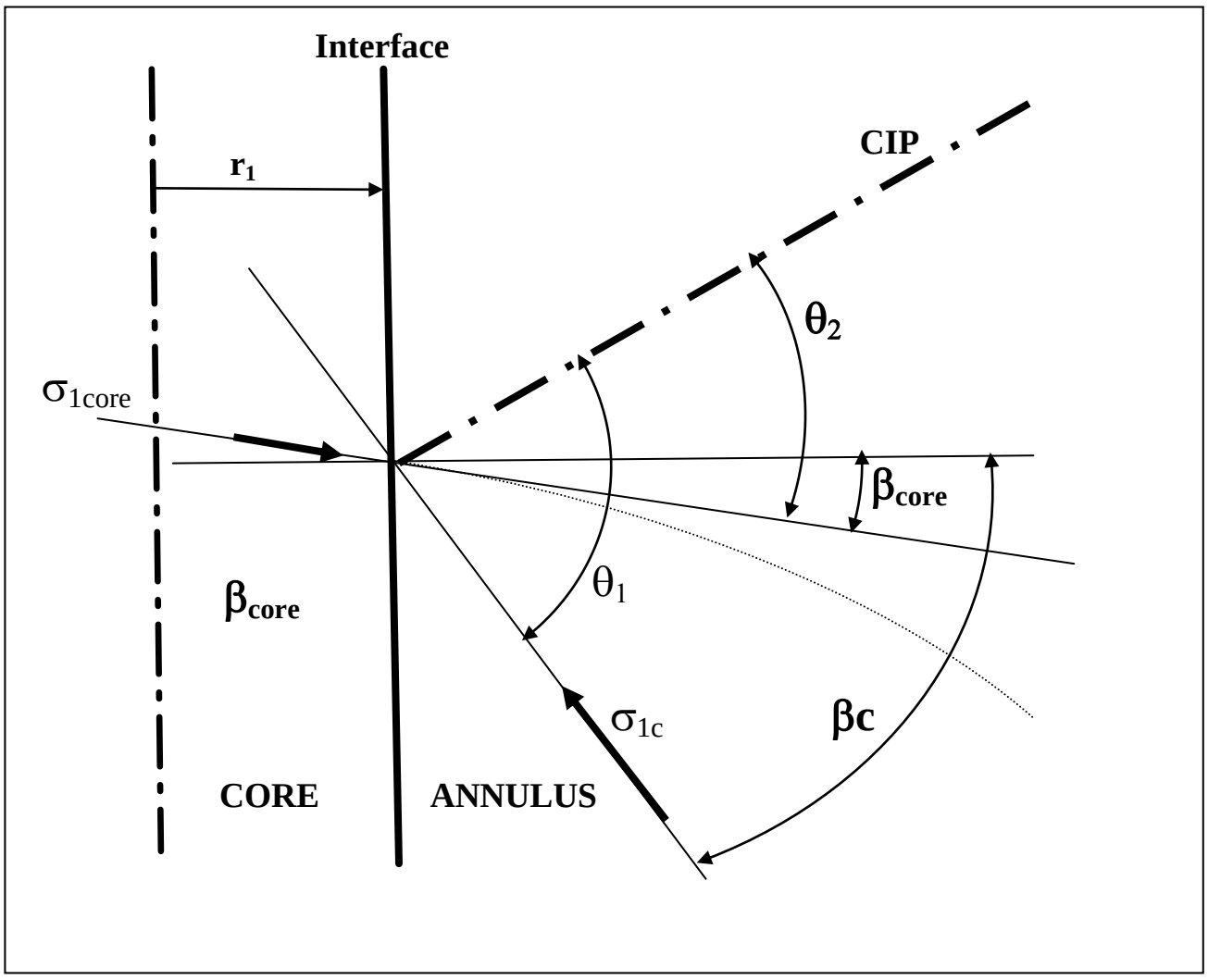

Figure 3 Mohr circles for the Common Interfacial Plane model: Mohr circles of the core wall and annulus wall

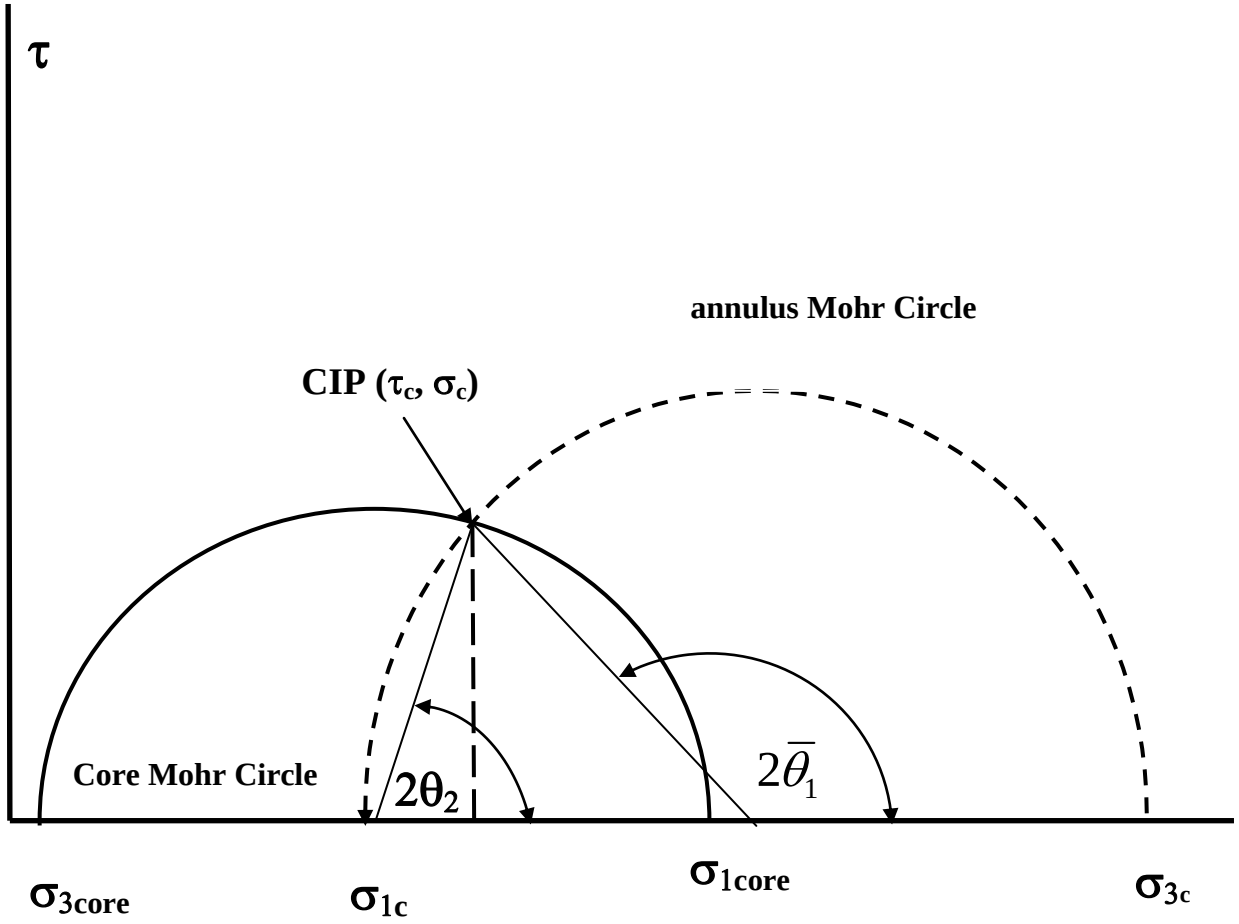

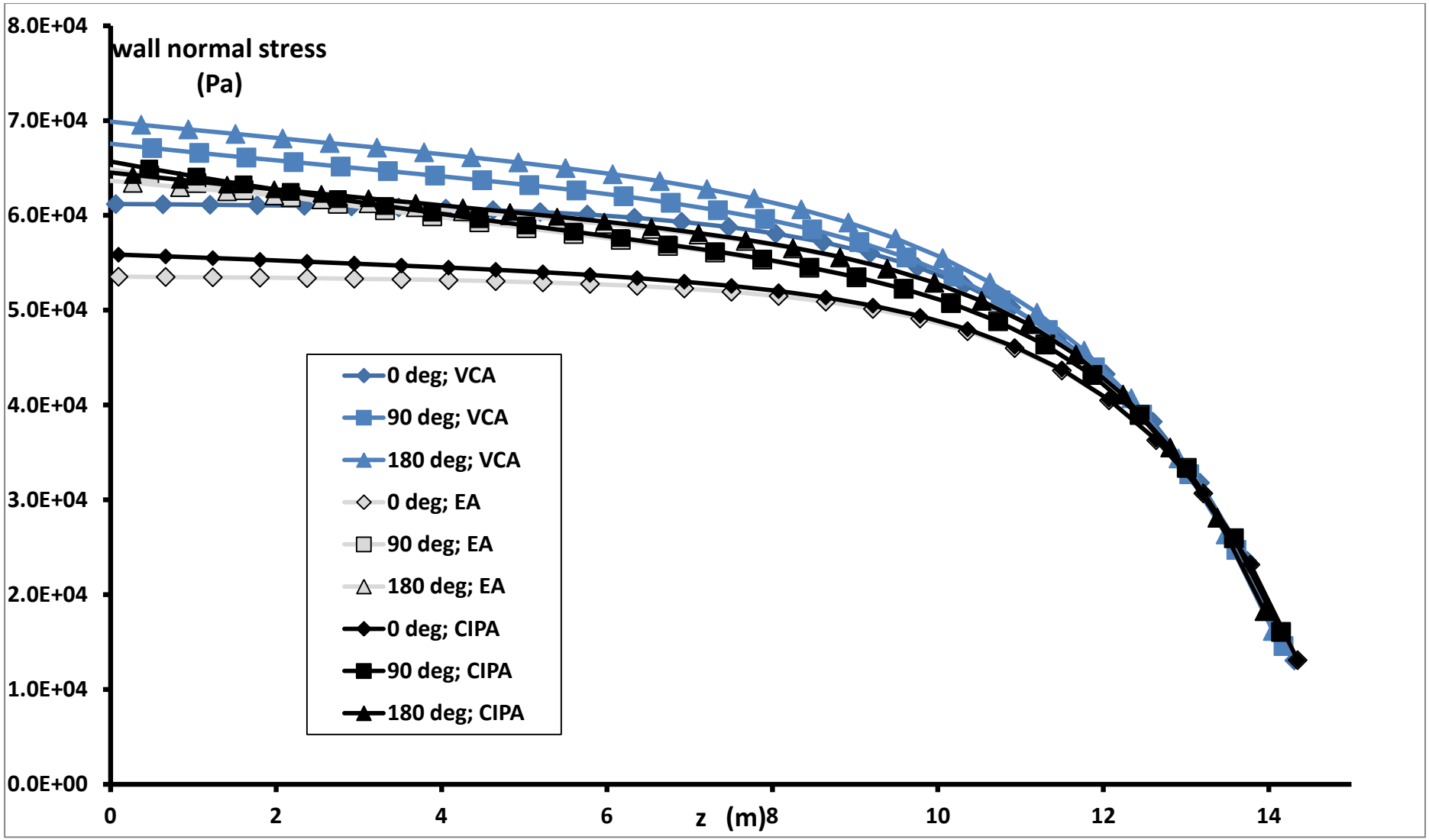

Figure 4

Effects of internal structure on wall normal stress. See Tables 1 & 2 for conditions. Figure 4a: different core models

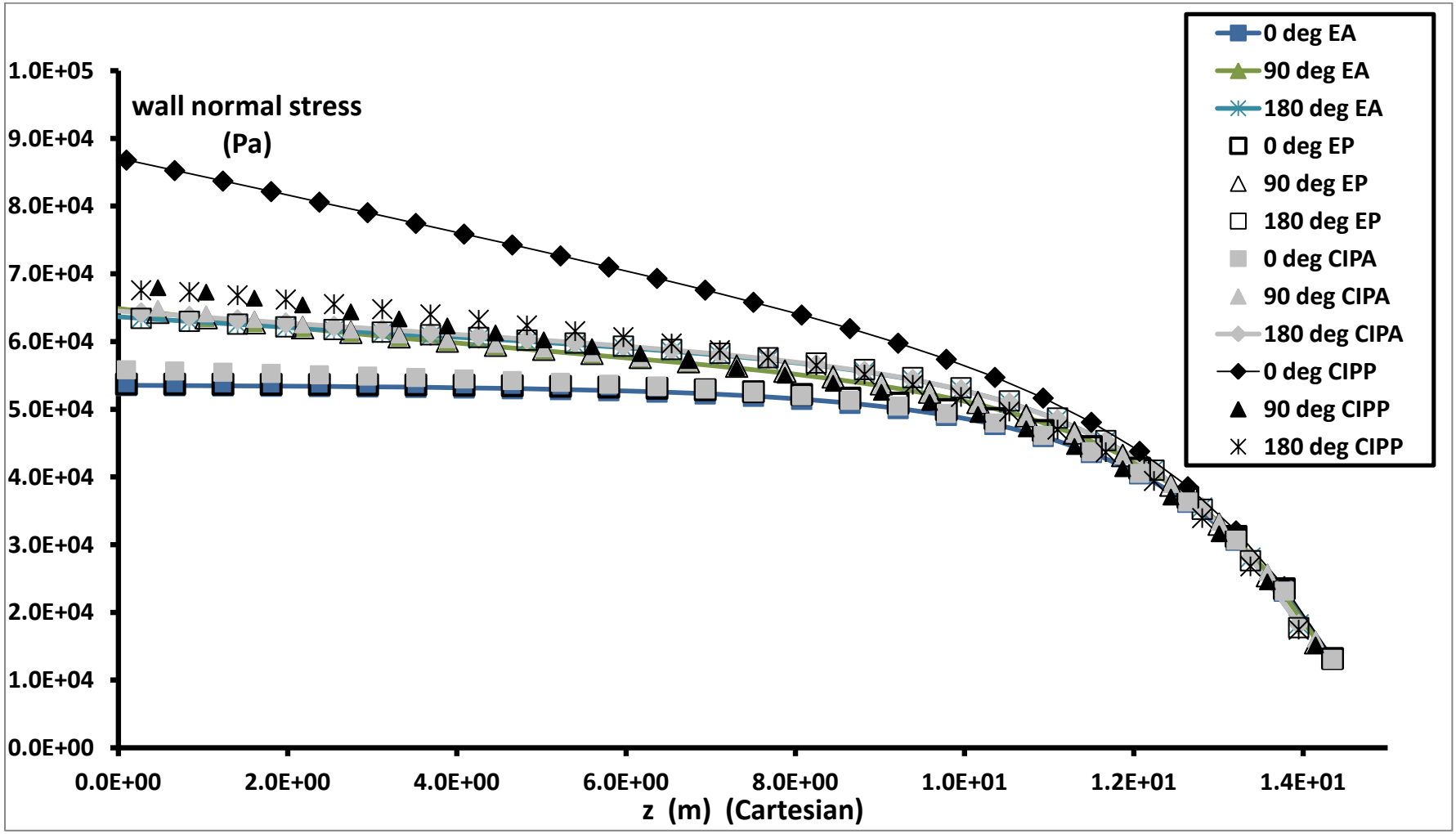

Figure 4 Effects of internal structure on wall normal stress.

Figure 4b: active and passive cores

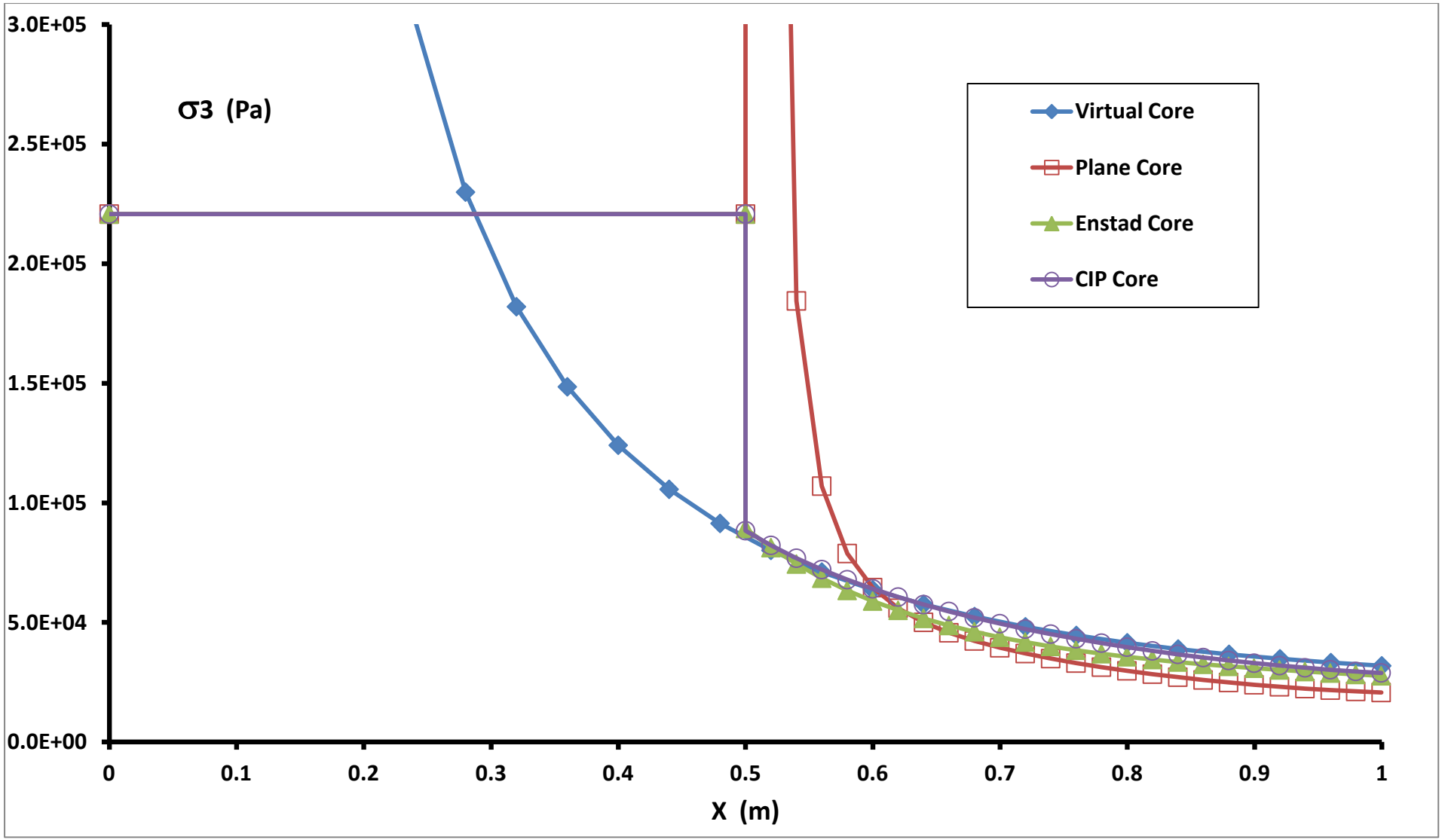

Figure 5 Internal stress distributions for different core models.

See Tables 1 & 2 for details. Figure 5a: σ_3 variation along the X-line at $\varepsilon_1=0^o$

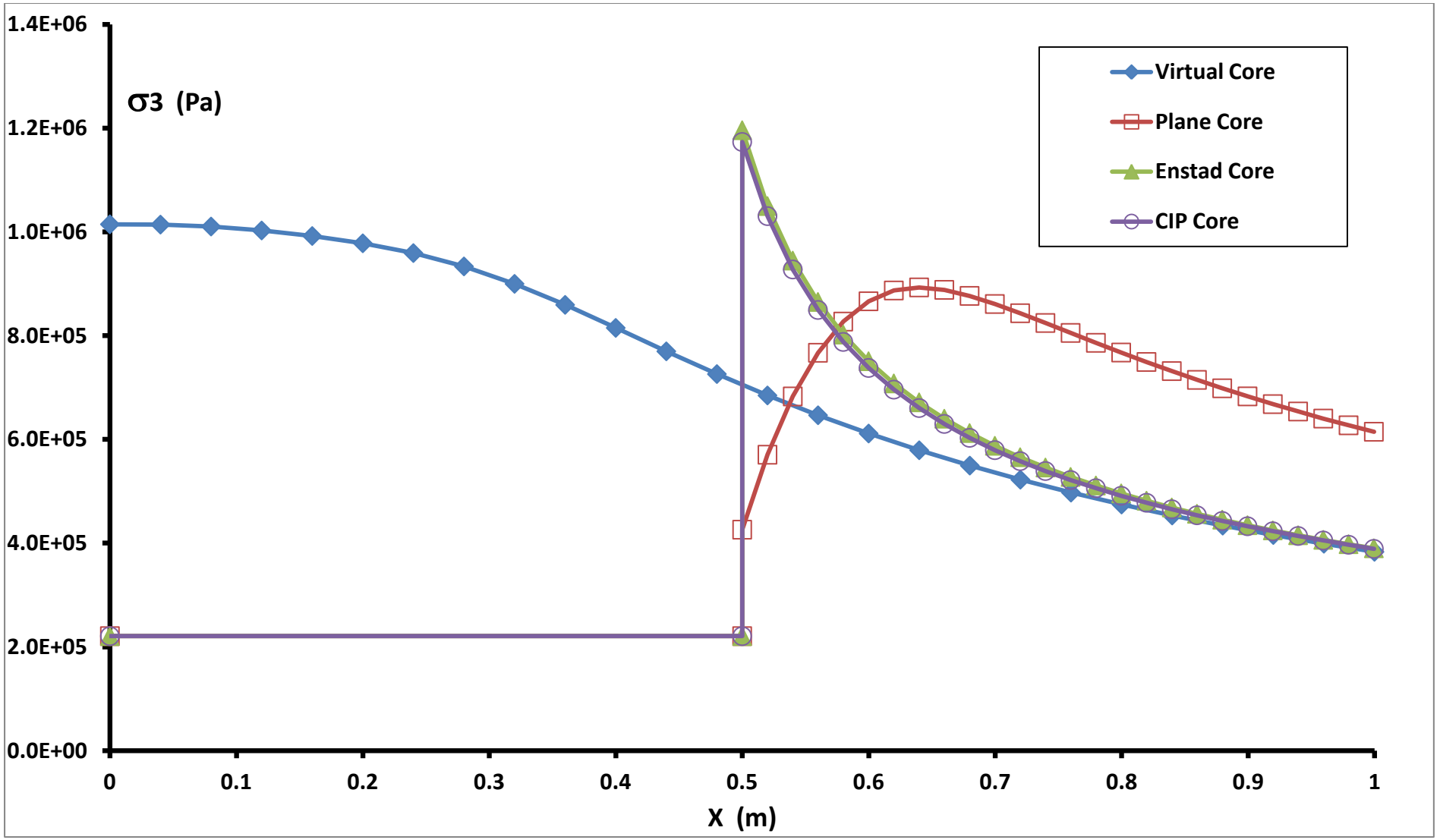

Figure 5 Internal stress distributions for different core models.

See Tables 1 & 2 for details . Figure 5b: σ_3 variation along the X-line at $\varepsilon_1=180^o$

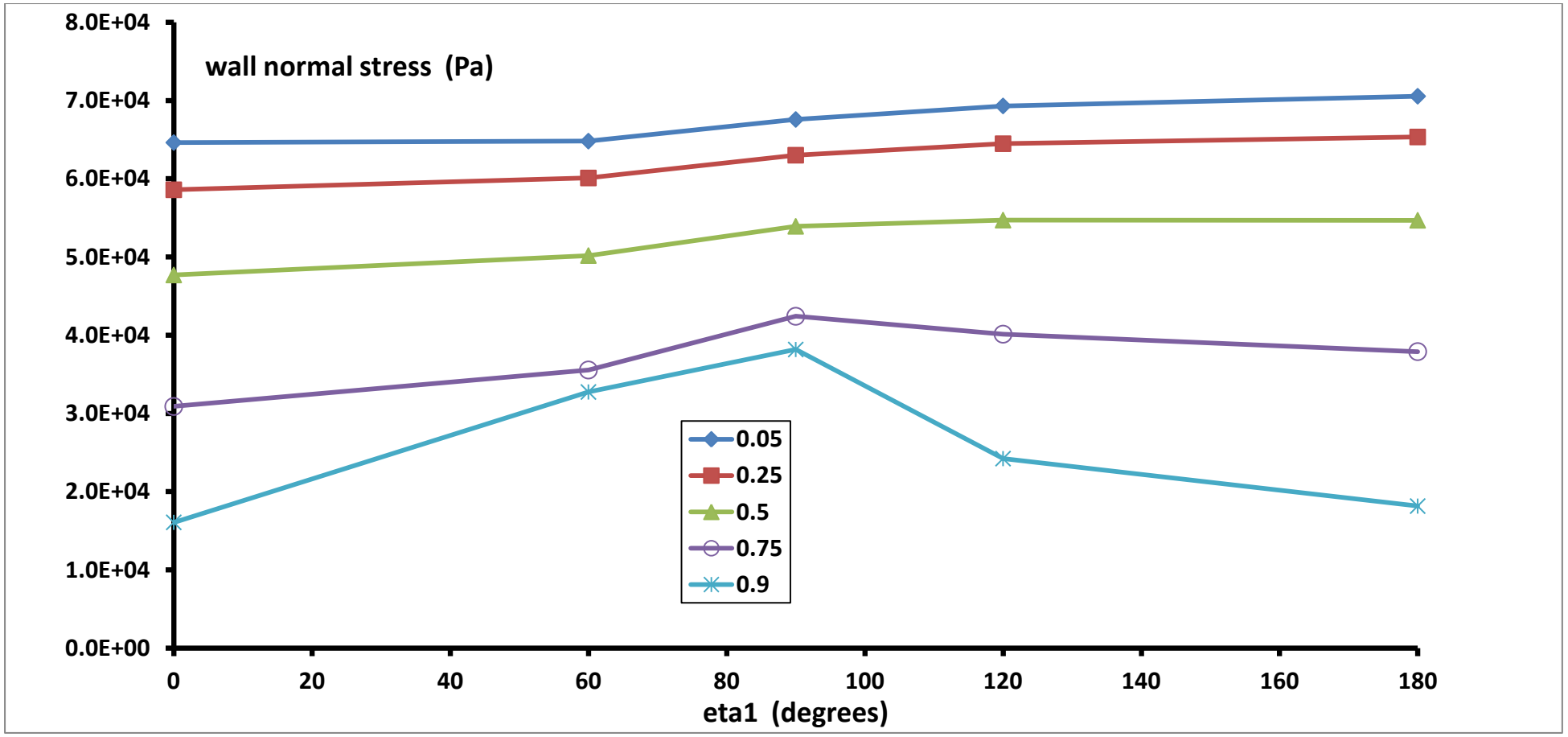

Figure 6 **Effects of core radius on wall normal stress: variation in wall normal stress with azimuthal variation ε_1, at depth (Z_o-Z) of 10m.**
Conditions as in Table 2, except:
Active core, J_{core}=0.333; h=1 m throughout
Enstad core with σ_1-continuity.
$\beta_w=8^o$; $\beta_c=\beta_{core}=3^o$

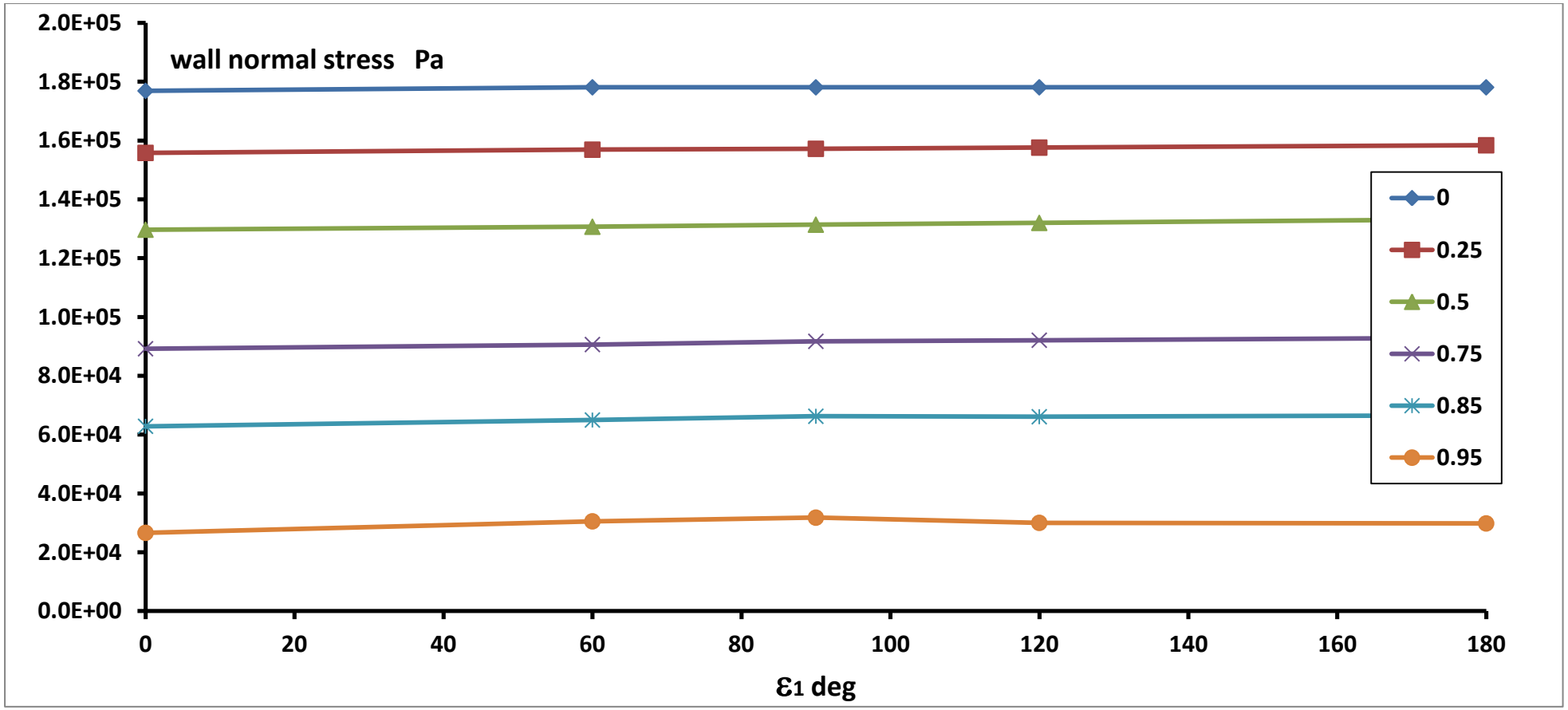

Figure 7 **Effects of Eccentricity (Ecc) on wall normal stress: variation in wall normal stress with azimuthal variation ε_1, at depth (Z_o-Z) of 10m.**
Conditions as in Table 2, except:
Passive core, $J_{core}=3$; $r_1=0.5$ m throughout
Enstad core with σ_1-continuity.
$\beta_w=10^o$; $\beta_c=\beta_{core}=3^o$

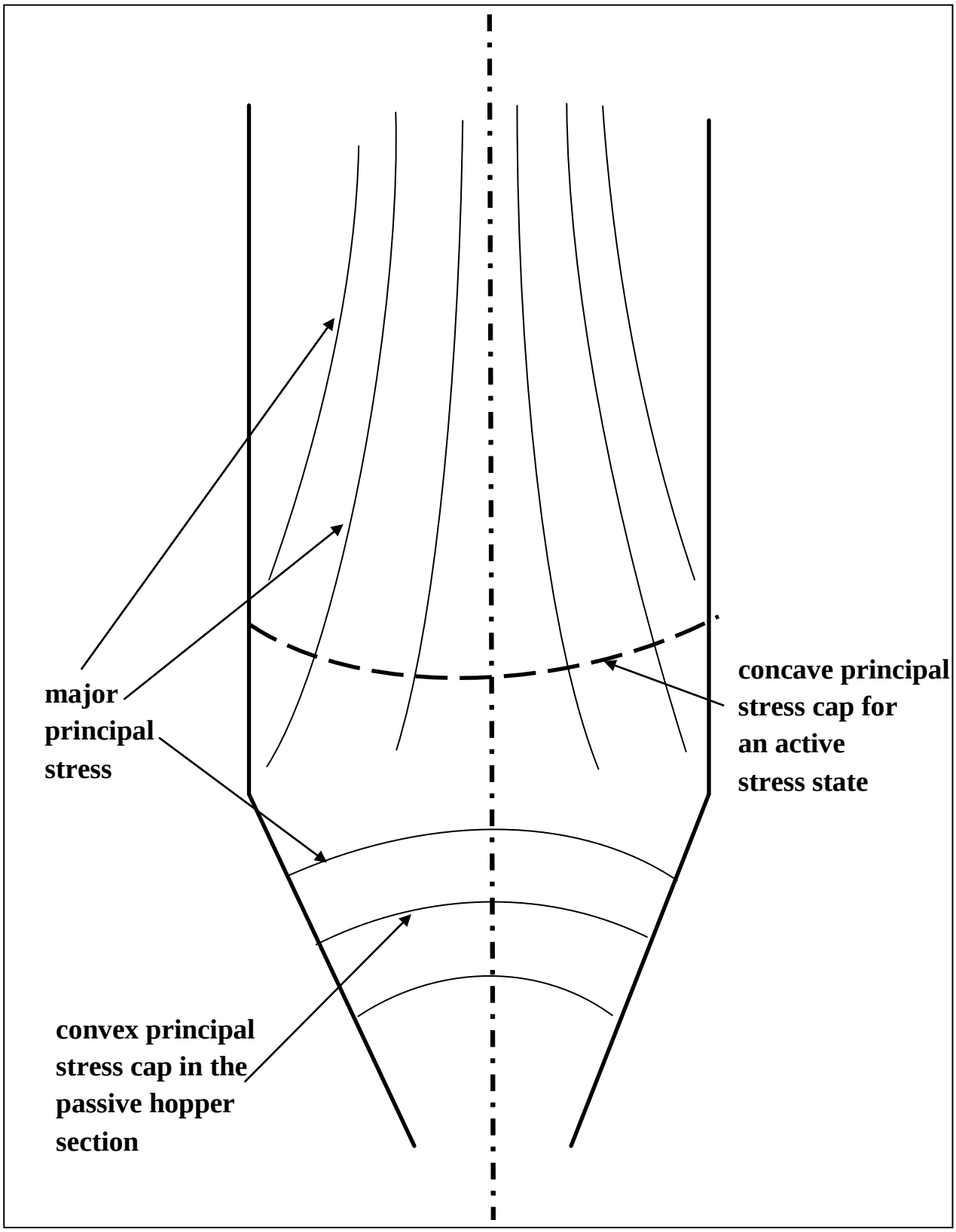

Figure 8 Concave principal stress cap half-surface

Figure 8a The accepted picture of lines of major principal stress in hopper/silo

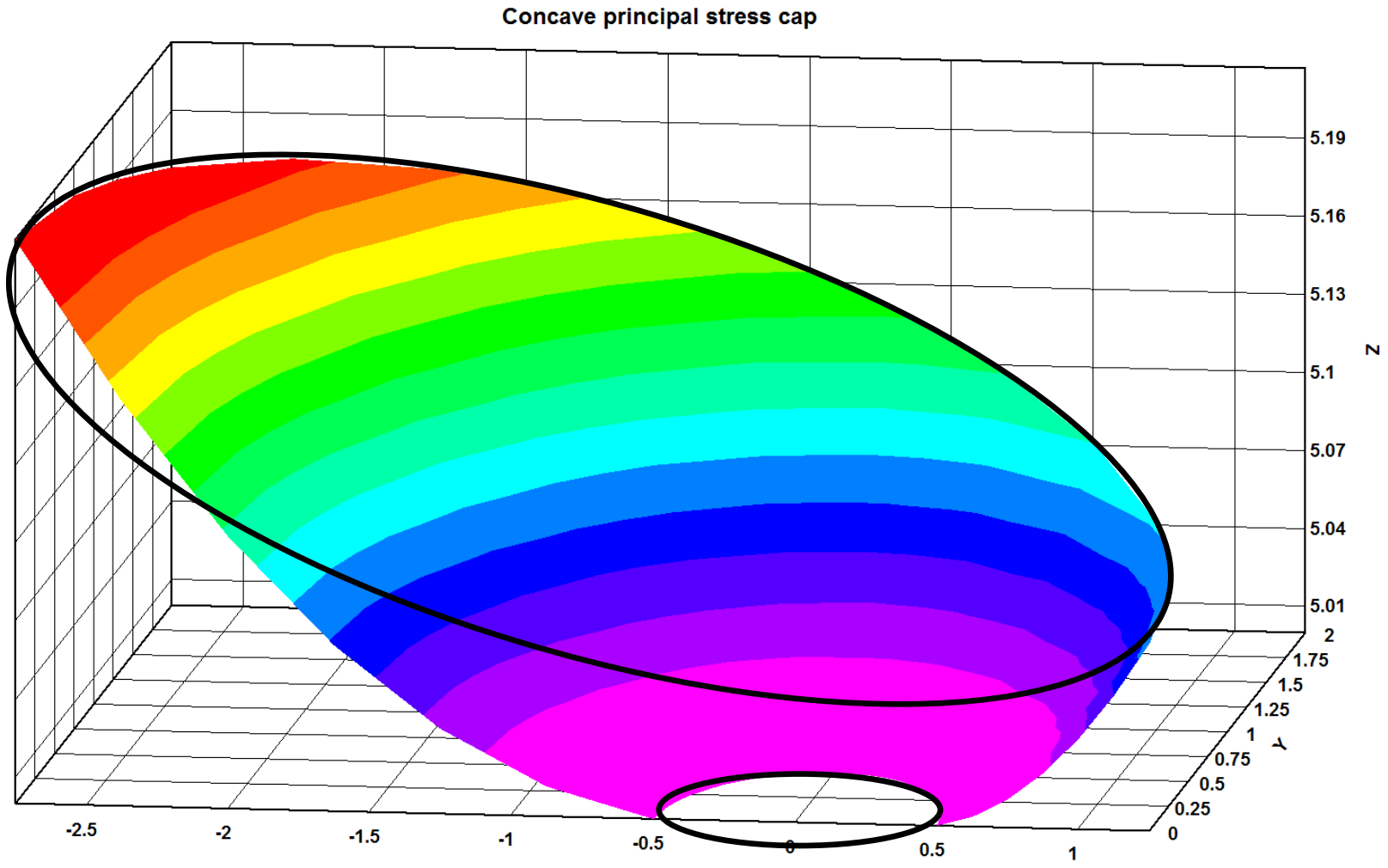

Figure 8b The shape of the principal stress cap surface half section; r_1=0.5; r_2=2m; $\beta_c=\beta_{core}=-1^o$; $\beta_w=-10^o$

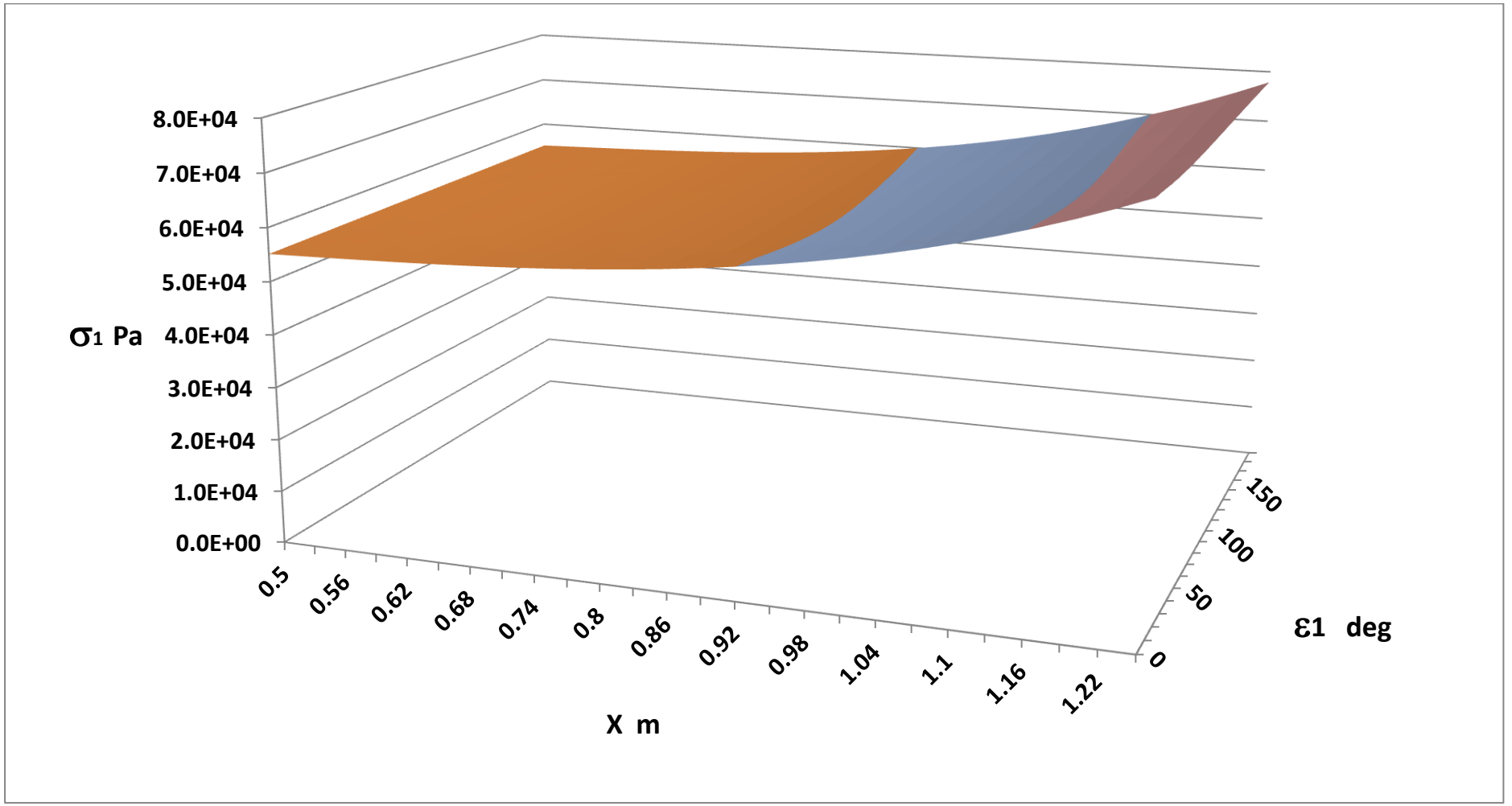

Figure 9 **Principal stress surfaces in X-ε_1 space at depth (Z_o - Z) of 10m. Geometry as in Figure 8. ρ=1500 kg/m^3; γ_1=-1; K_w=0.95; γ_2=-γ_1/K_w; Ecc=0.5.**

Figure 9a σ_1 in X-ε_1 space

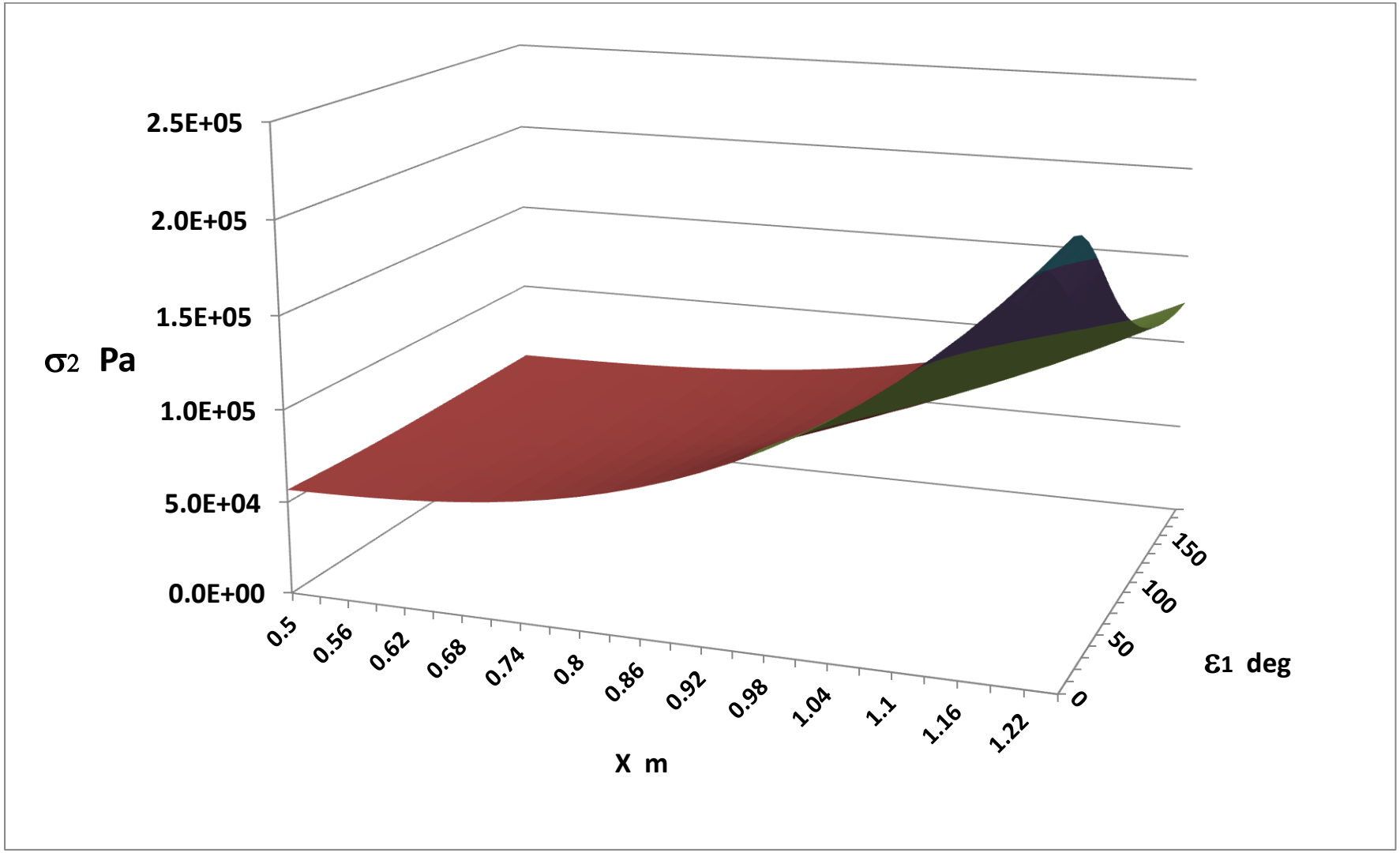

Figure 9b σ_2 in X-ε_1 space

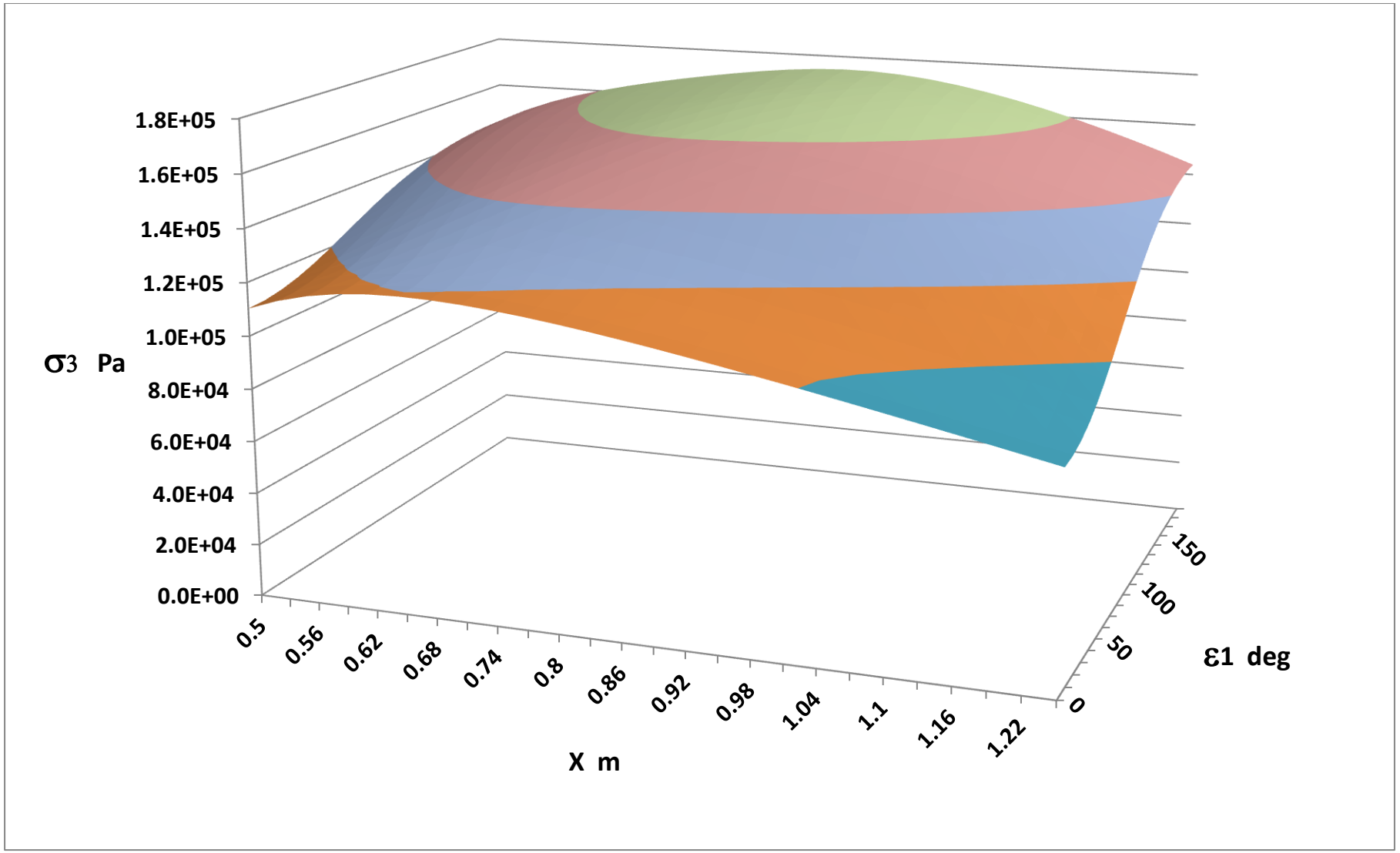

Figure 9c σ_3 in X-ε_1 space

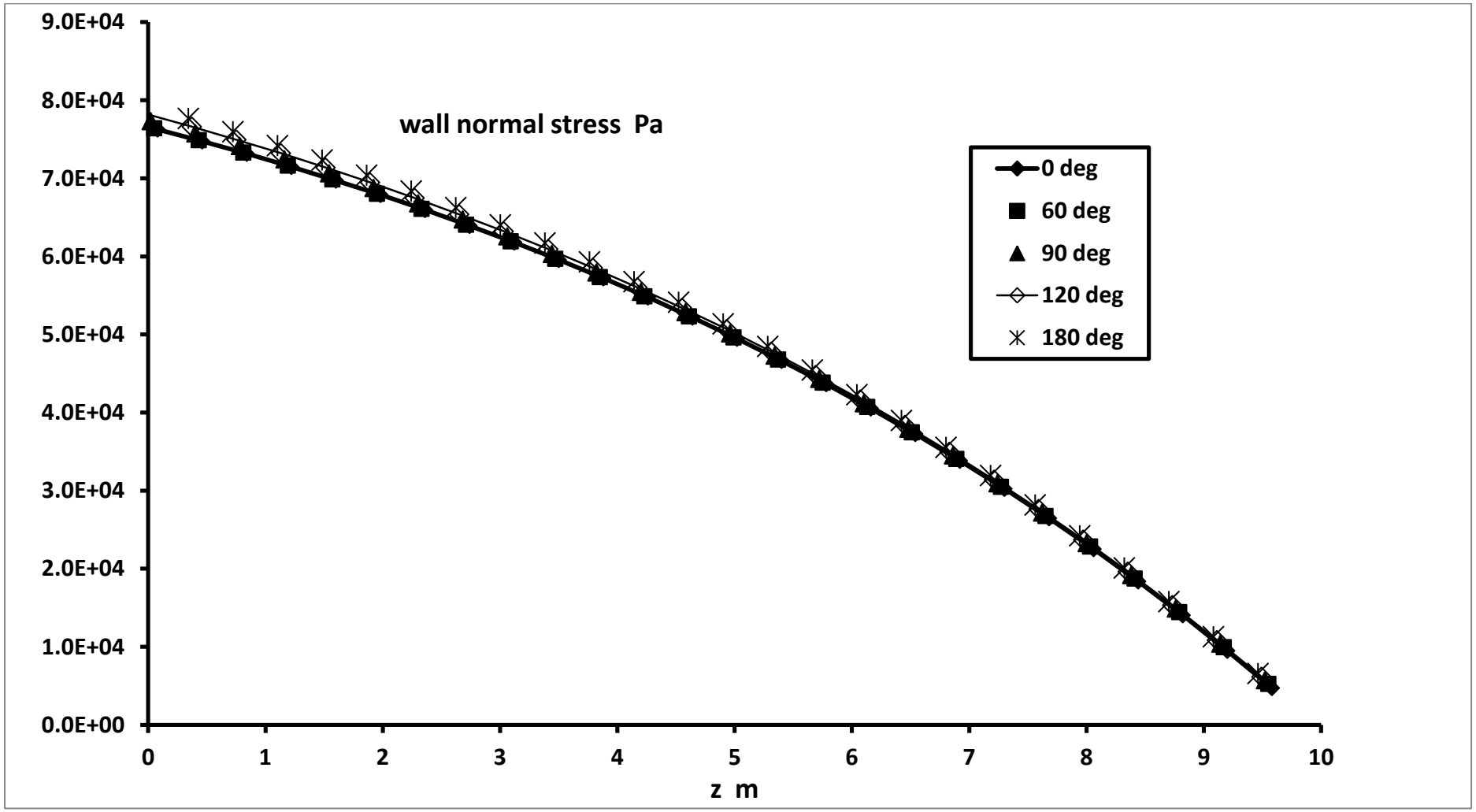

Figure 10 Wall stresses for conditions in Figures 8 & 9.
Figure 10a wall normal stress versus z

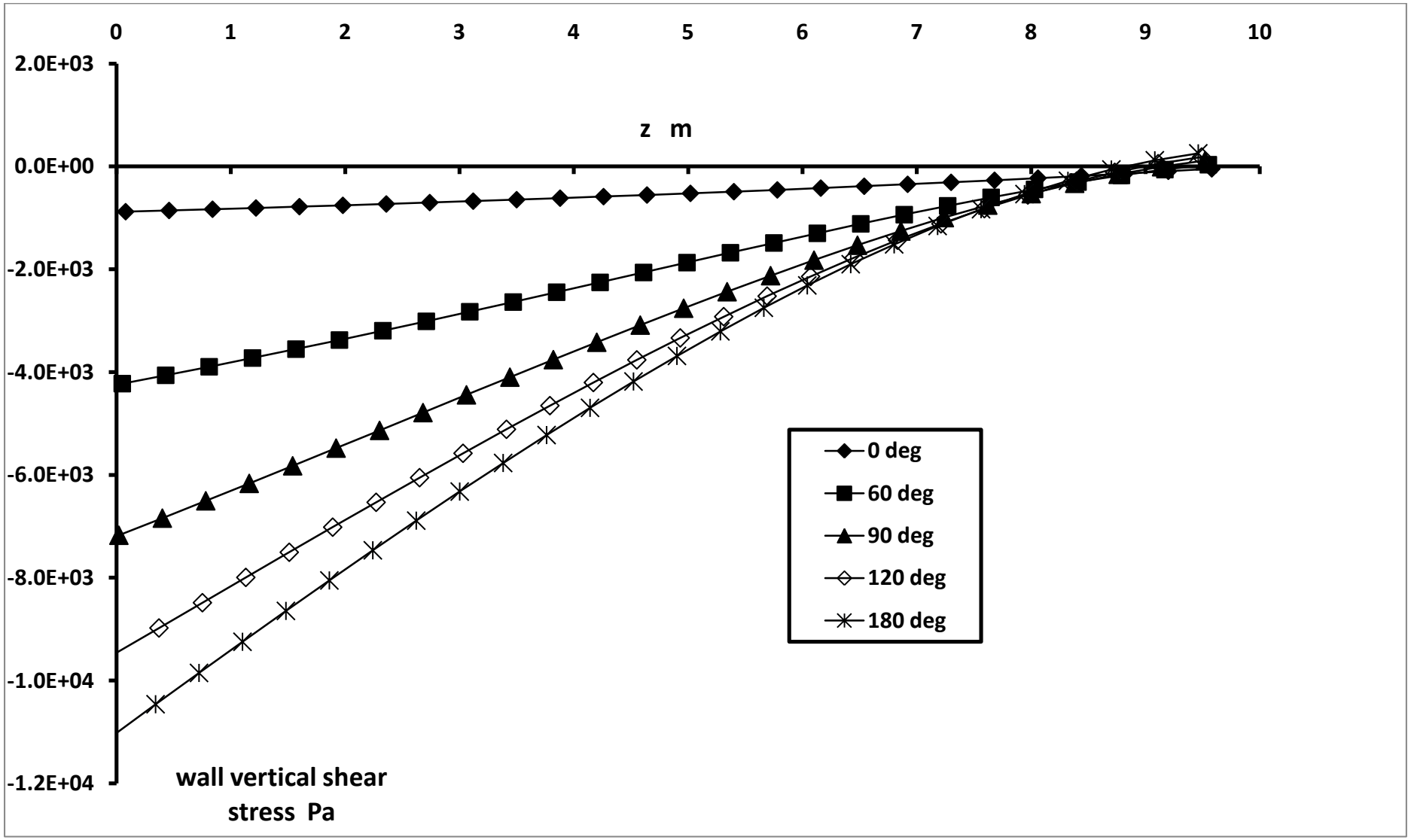

Figure 10b wall vertical shear stress versus z

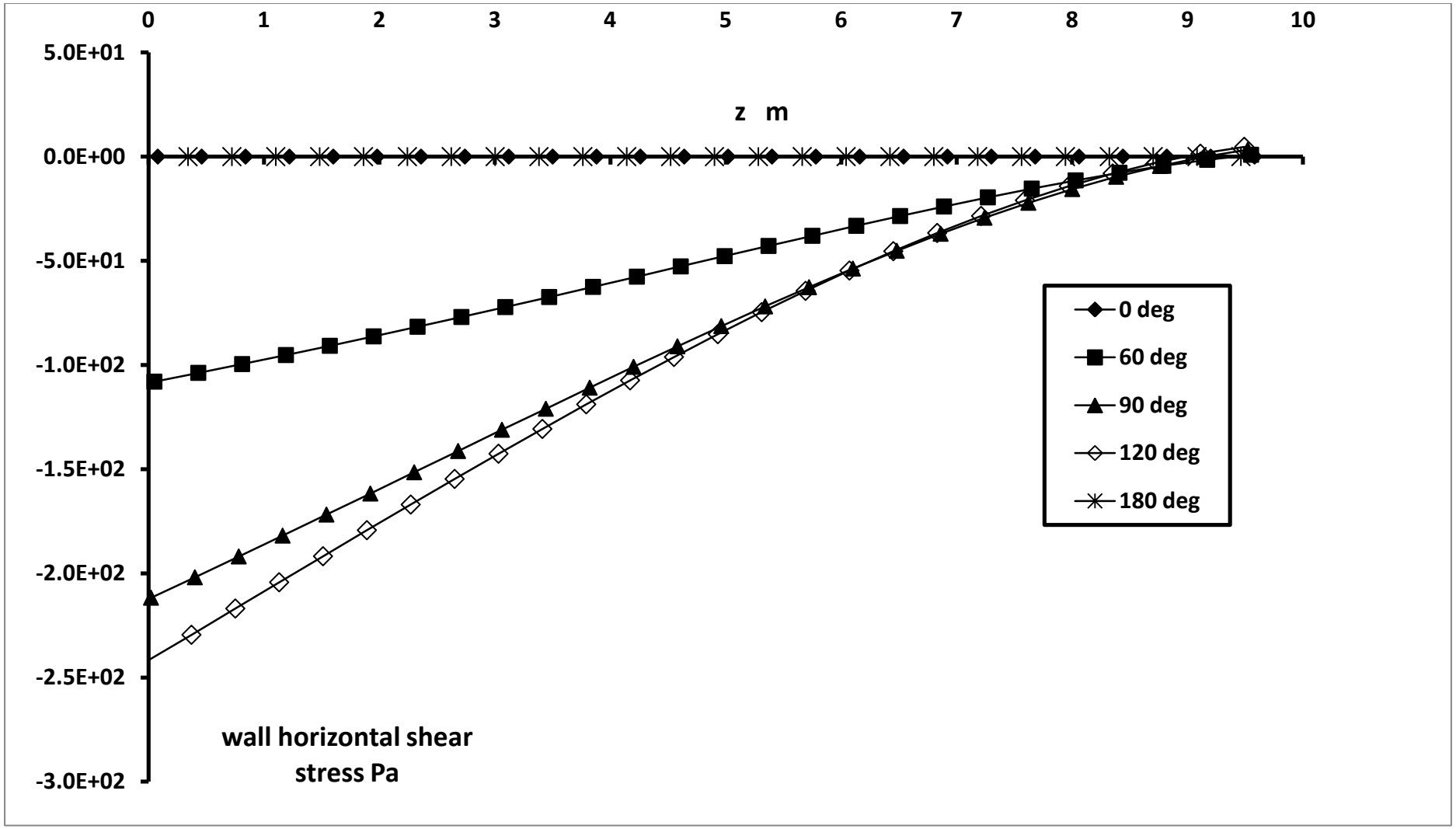

Figure 10c wall horizontal shear stress

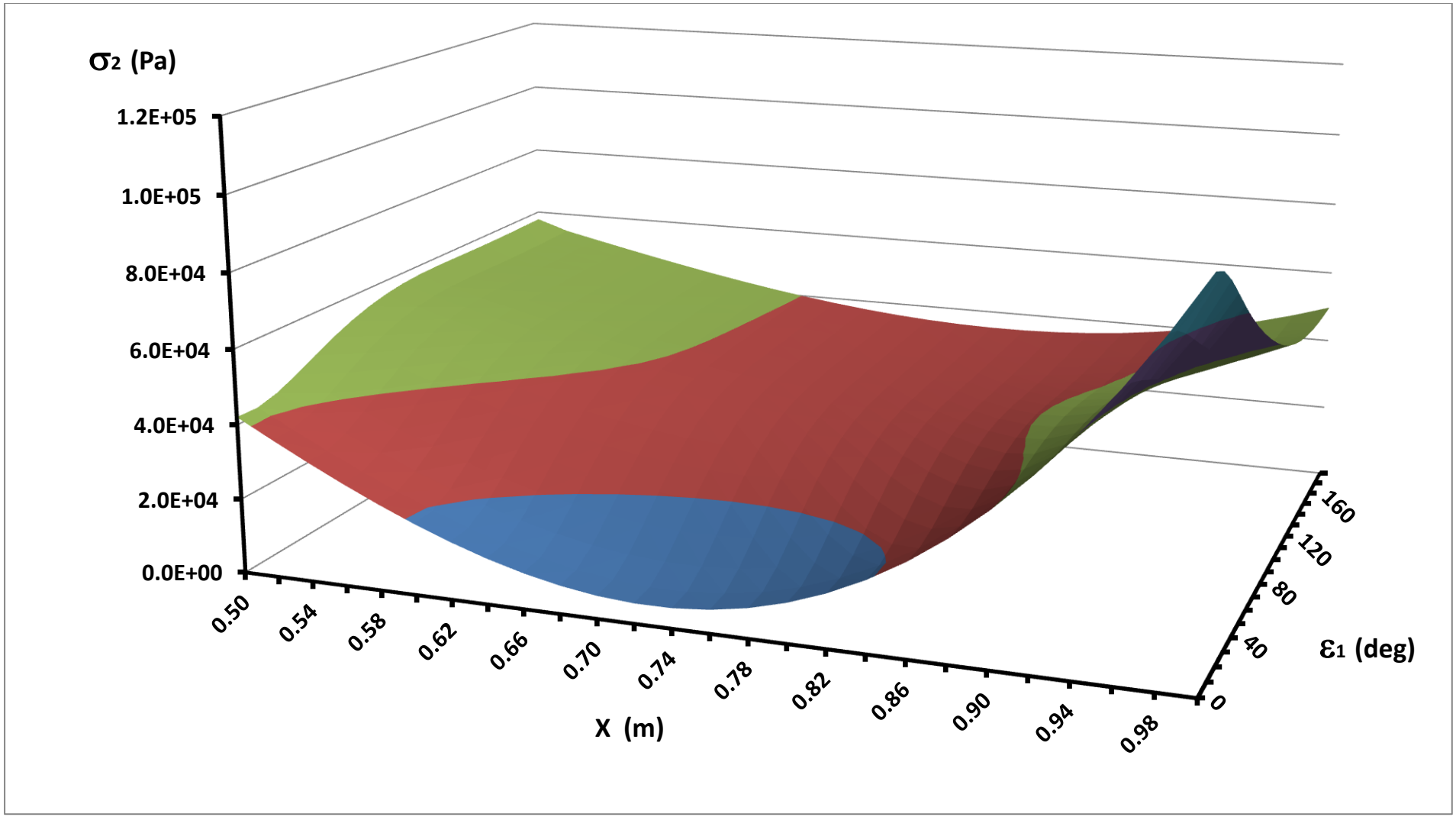

Figure 11 Principal stress σ_2 over the principal stress cap at depth $(Z_o\text{-}Z)$=15m. The conditions are given in Table 2.

Figure 11a CIPA

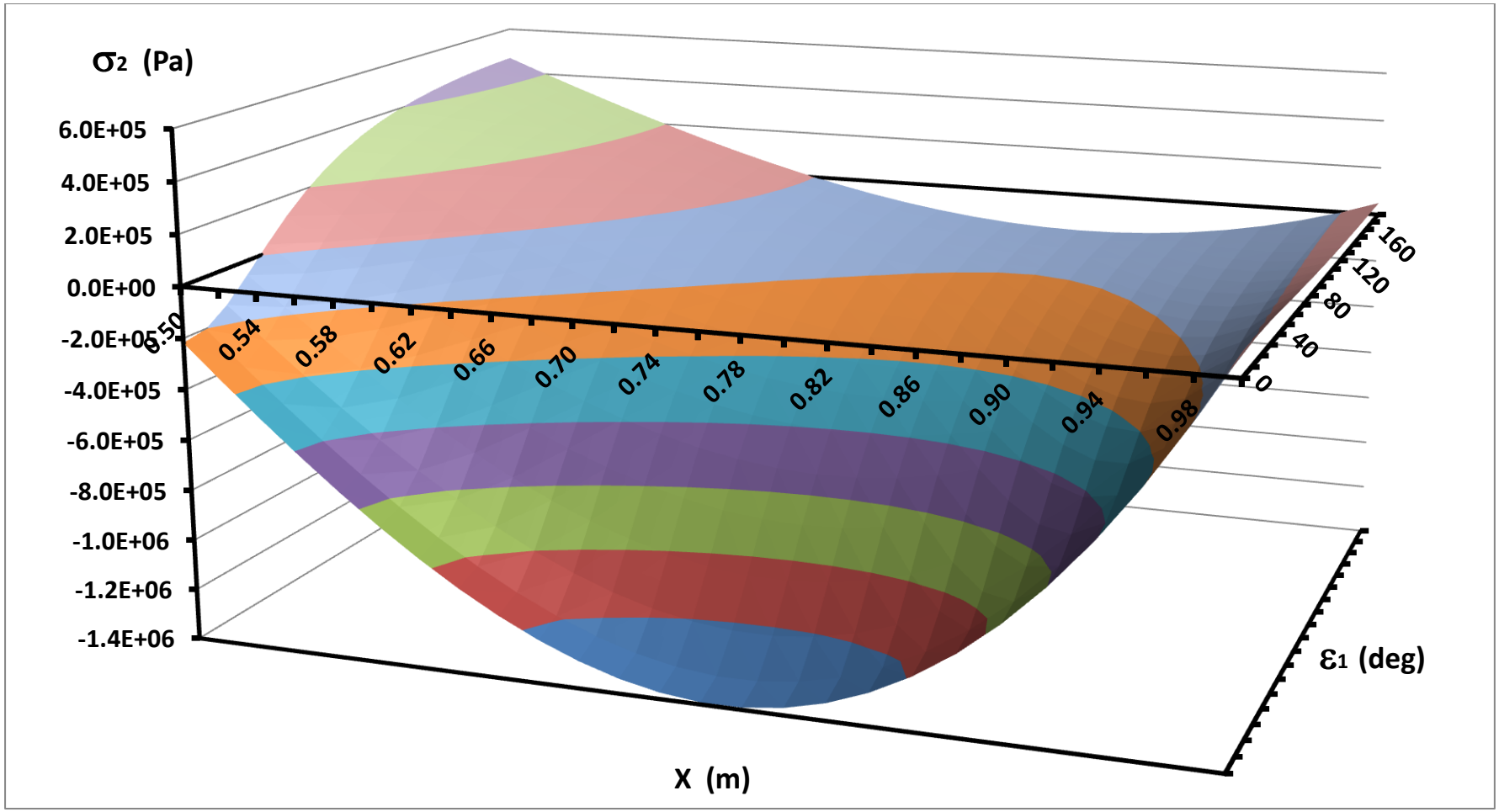

Figure 11 **Principal stress σ_2 over the principal stress cap at depth $(Z_o\text{-}Z)$=15m. The conditions are given in Table 2.**

Figure 11b CIPP

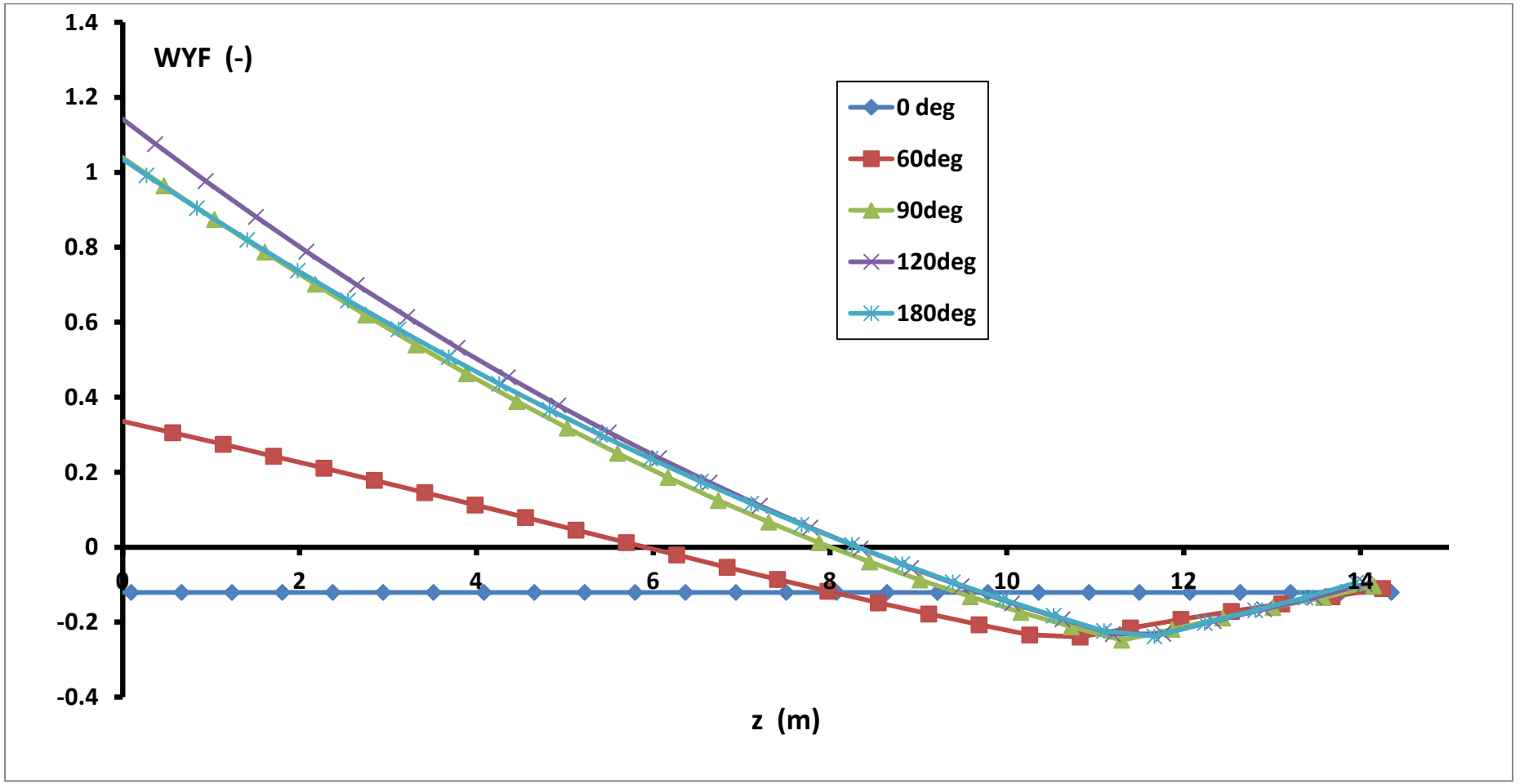

Figure 12

Wall Yield Function (WYF) as a function of ε_1 and depth for the simulation EPA in Figure 4. See Figure 2 for details

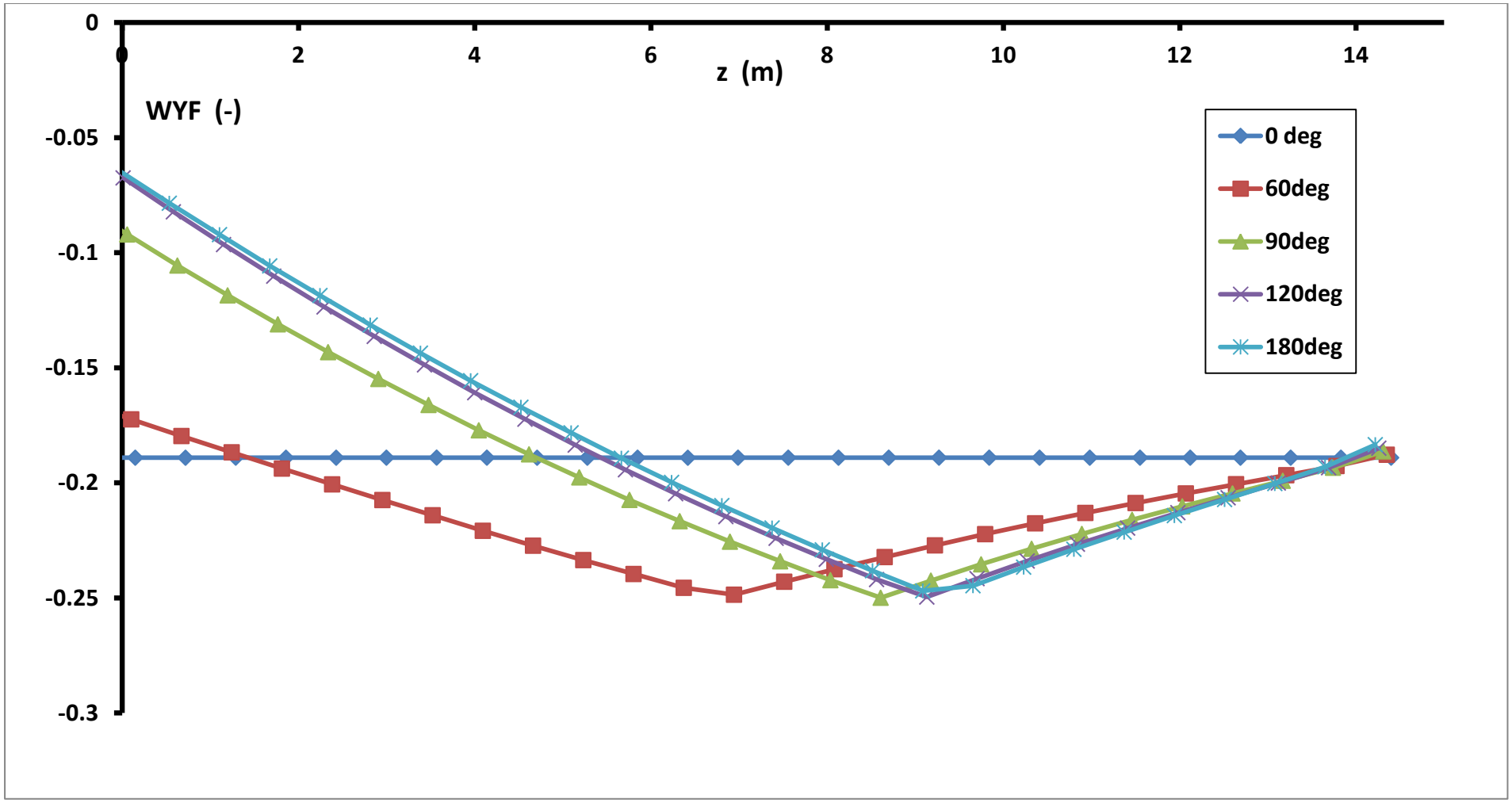

Figure 13

Wall Yield Function (WYF) as a function of ε_1 and depth for the simulation of revised conditions for the ECA simulation. Conditions as in Figure 4, Table 2 and Figure 12, except: $\beta_w=7^o$; $\beta_c=\beta_{core}=3.5^o$

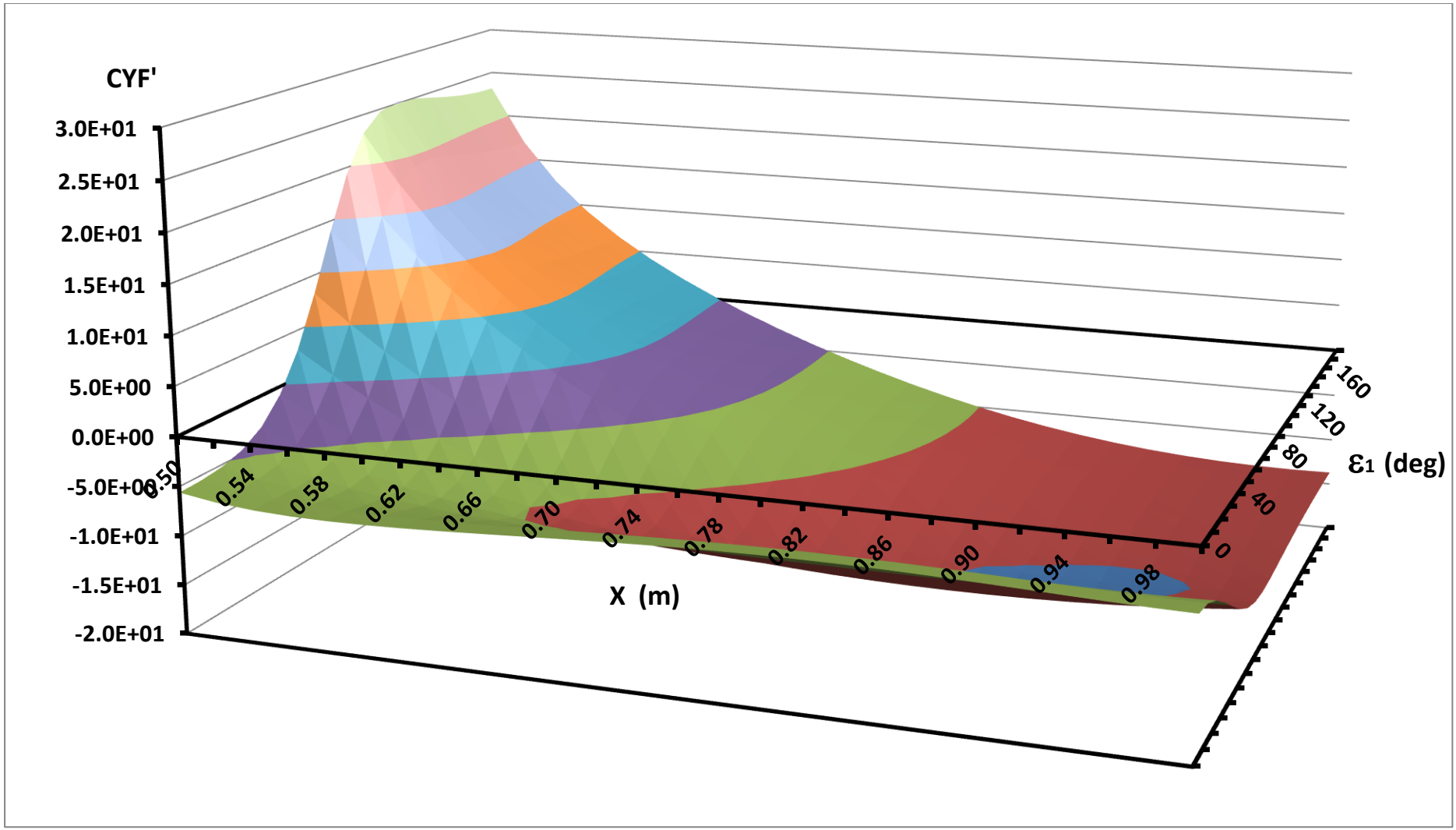

Figure 14

CYF' for the principal stress cap at depth (Z_o-Z) of 15m. Conditions as shown in Figure 13.

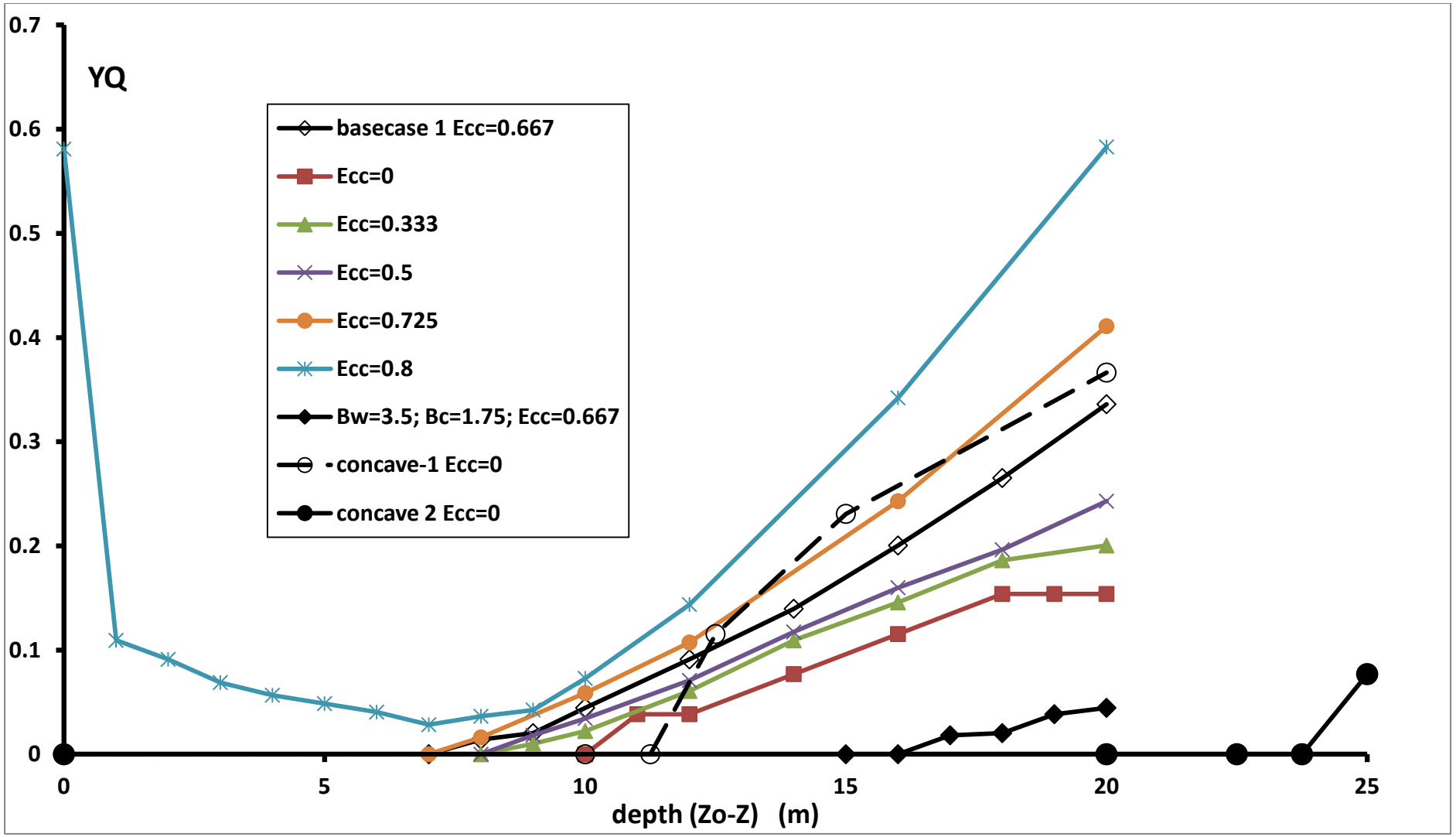

Figure 15

The Yield Quotient (YQ) for a range of simulations, including those in Figures 13 & 14. For details see Table 3.

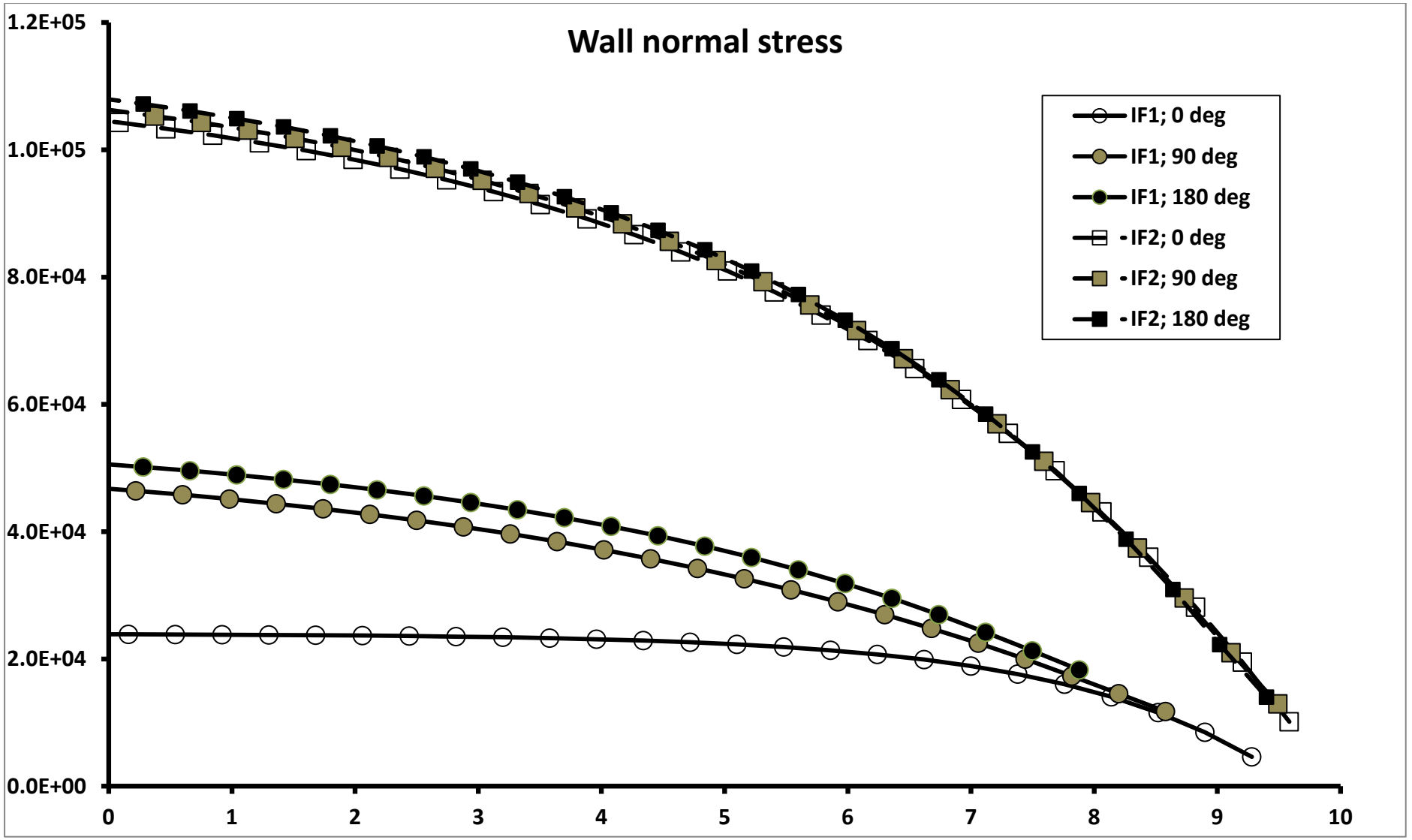

Figure 16 Wall stresses for a silo at incipient core-flow. For conditions see Table 4

Figure 16a wall normal stress versus z

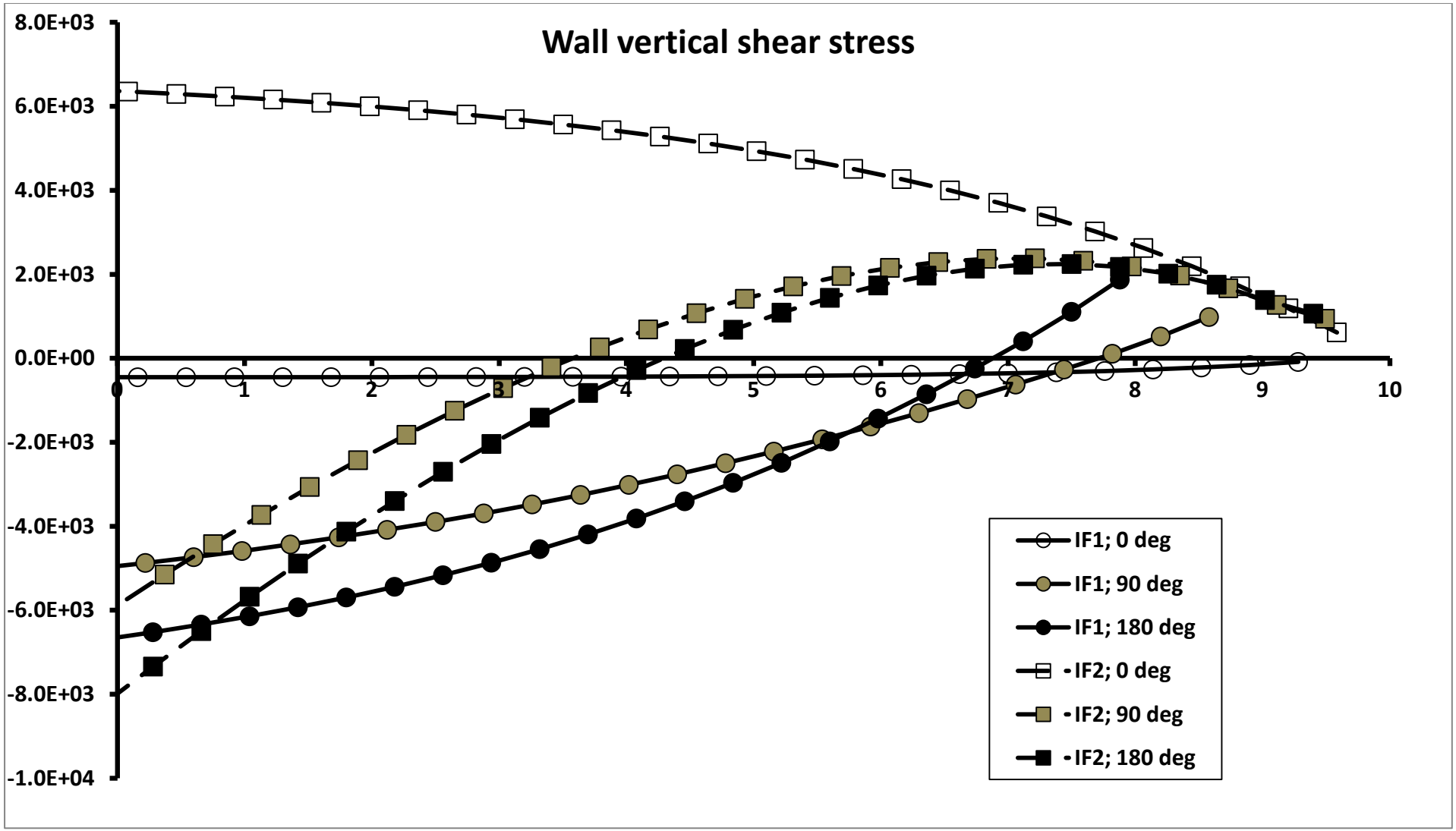

Figure 16 Wall stresses for a silo at incipient core-flow. For conditions see Table 4

Figure 16b wall vertical shear stress versus z

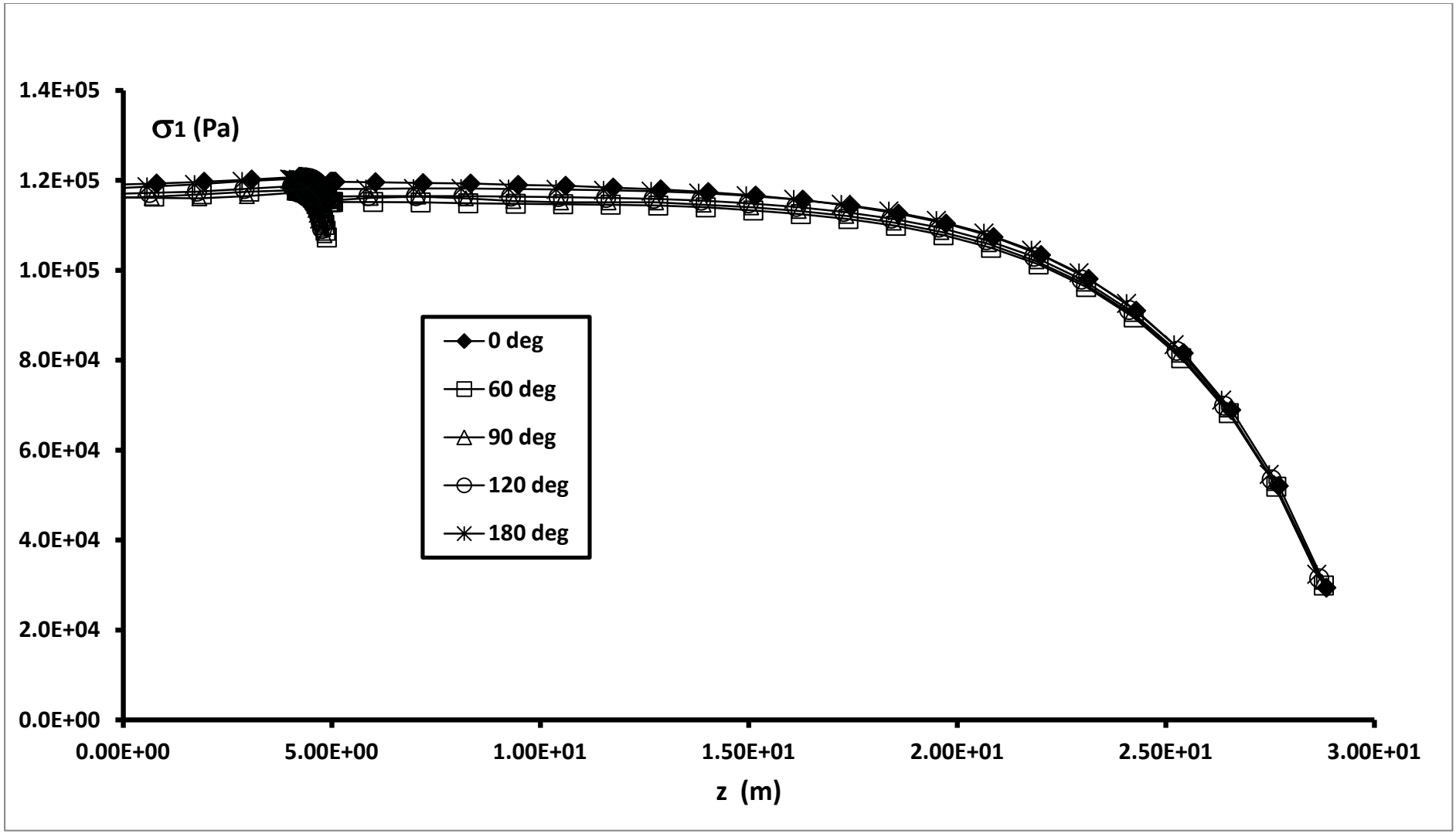

Figure 17 Switch stresses in a silo section 3m radius and 30m tall: conditions shown in Table 5

Figure 17a Principal stress σ_1 versus Cartesian coordinate z

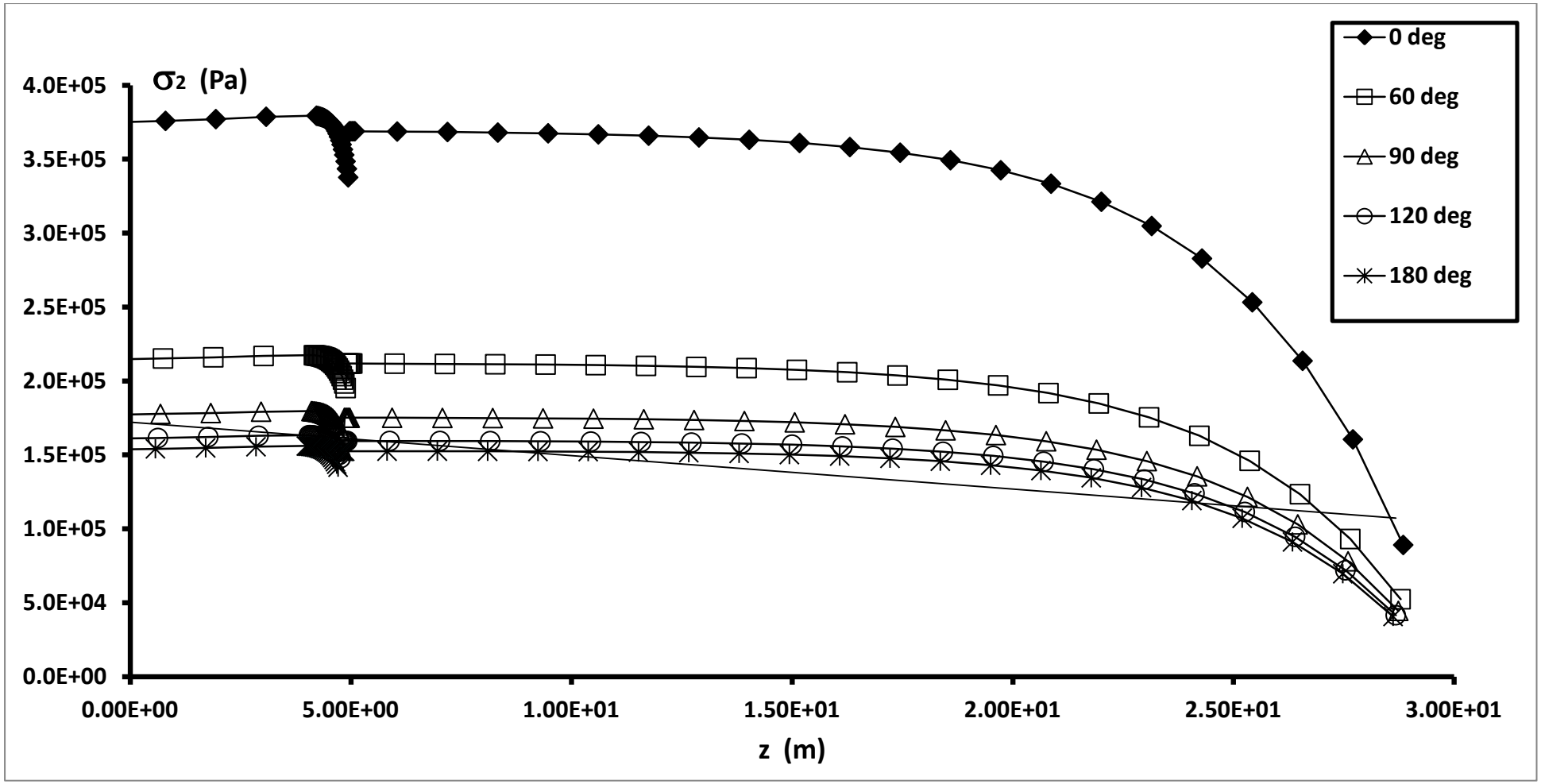

Figure 17 Switch stresses in a silo section 3m radius and 30m tall: conditions shown in Table 5

Figure 17b Principal stress σ_2 versus Cartesian coordinate z

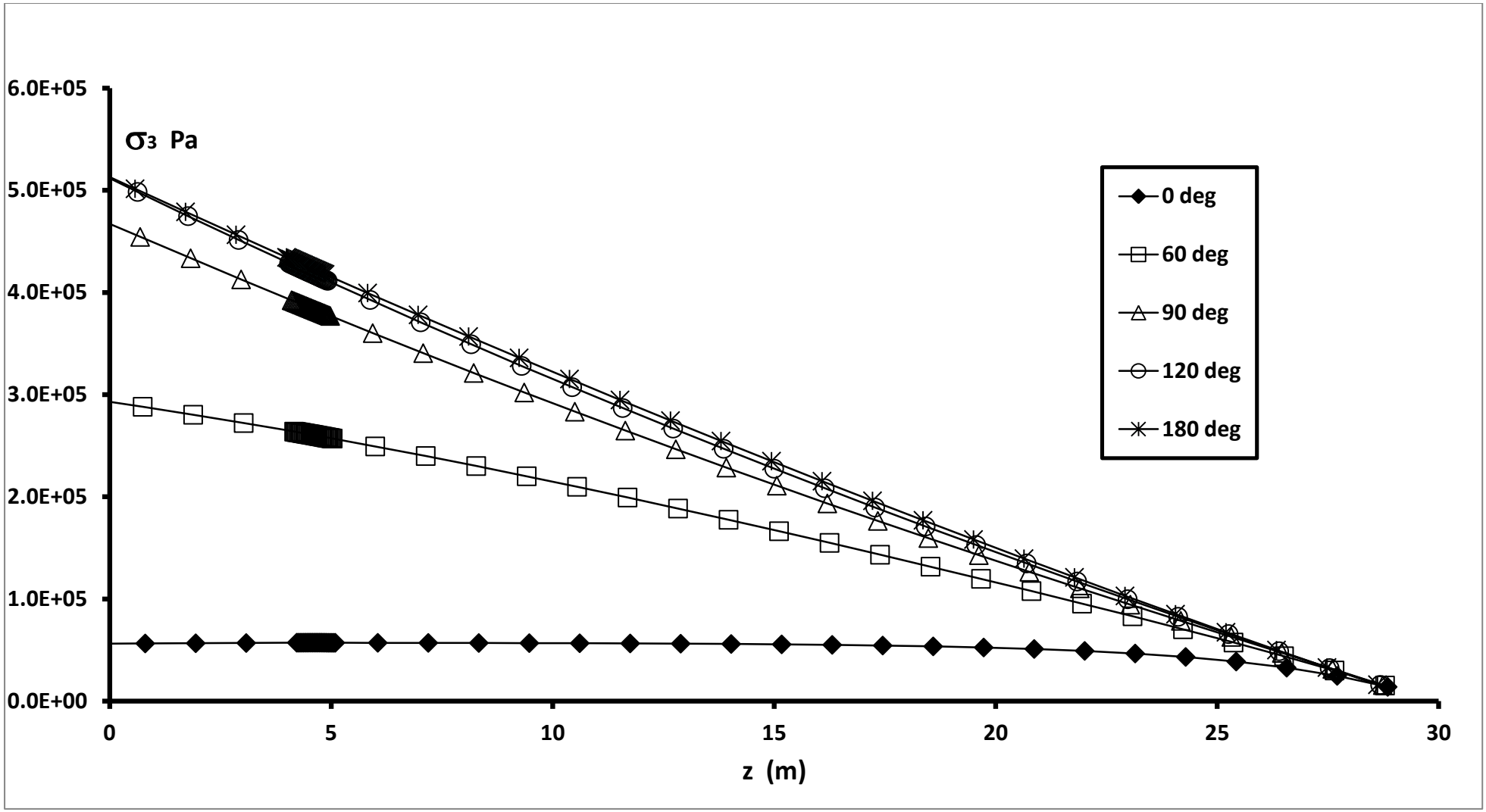

Figure 17 Switch stresses in a silo section 3m radius and 30m tall: conditions shown in Table 5

Figure 17c Principal stress σ_3 versus Cartesian coordinate z

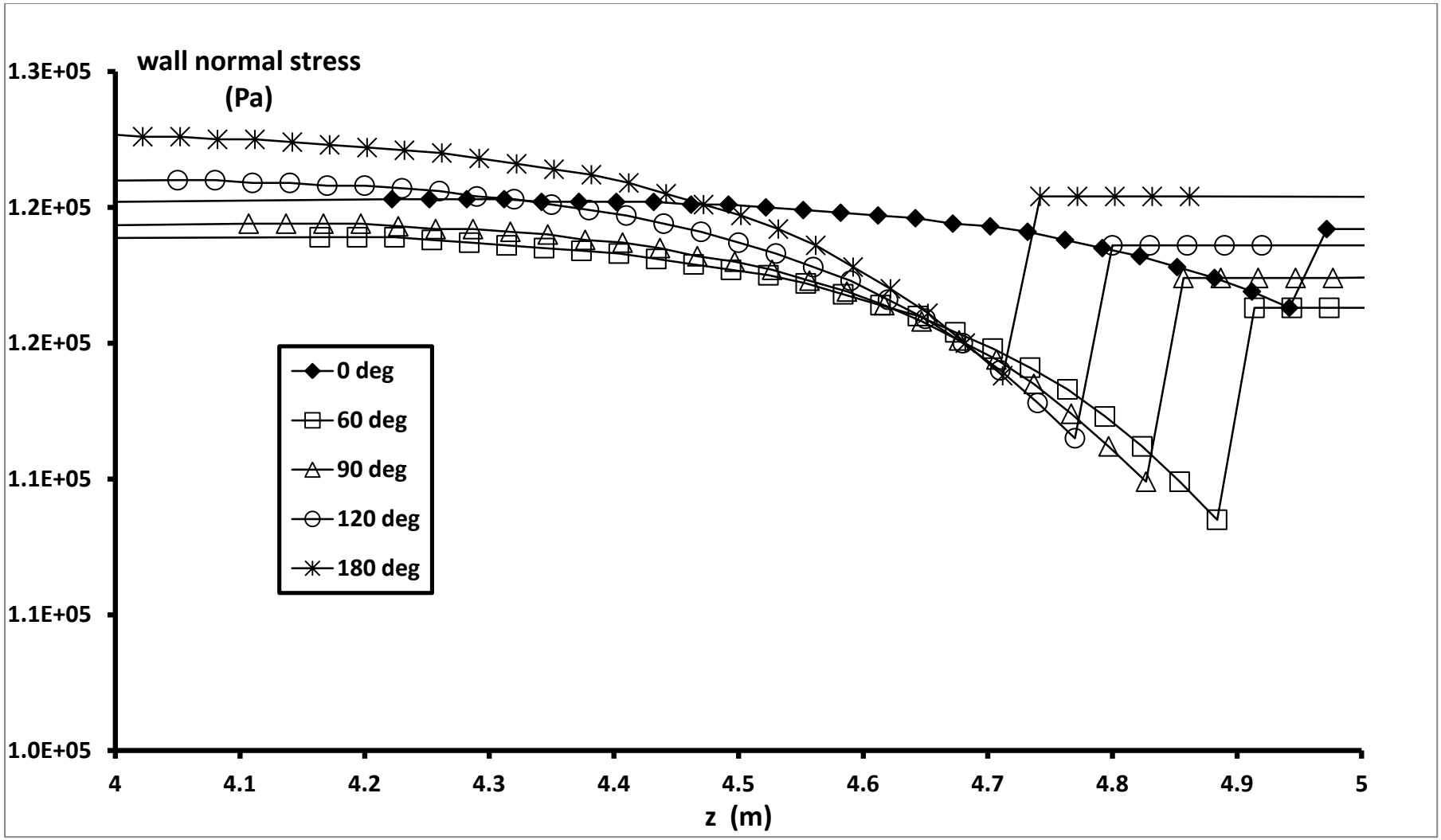

Figure 17 Switch stresses in a silo section 3m radius and 30m tall: conditions shown in Table 5

Figure 17d Wall normal stress in the region of the switch versus Cartesian coordinate z

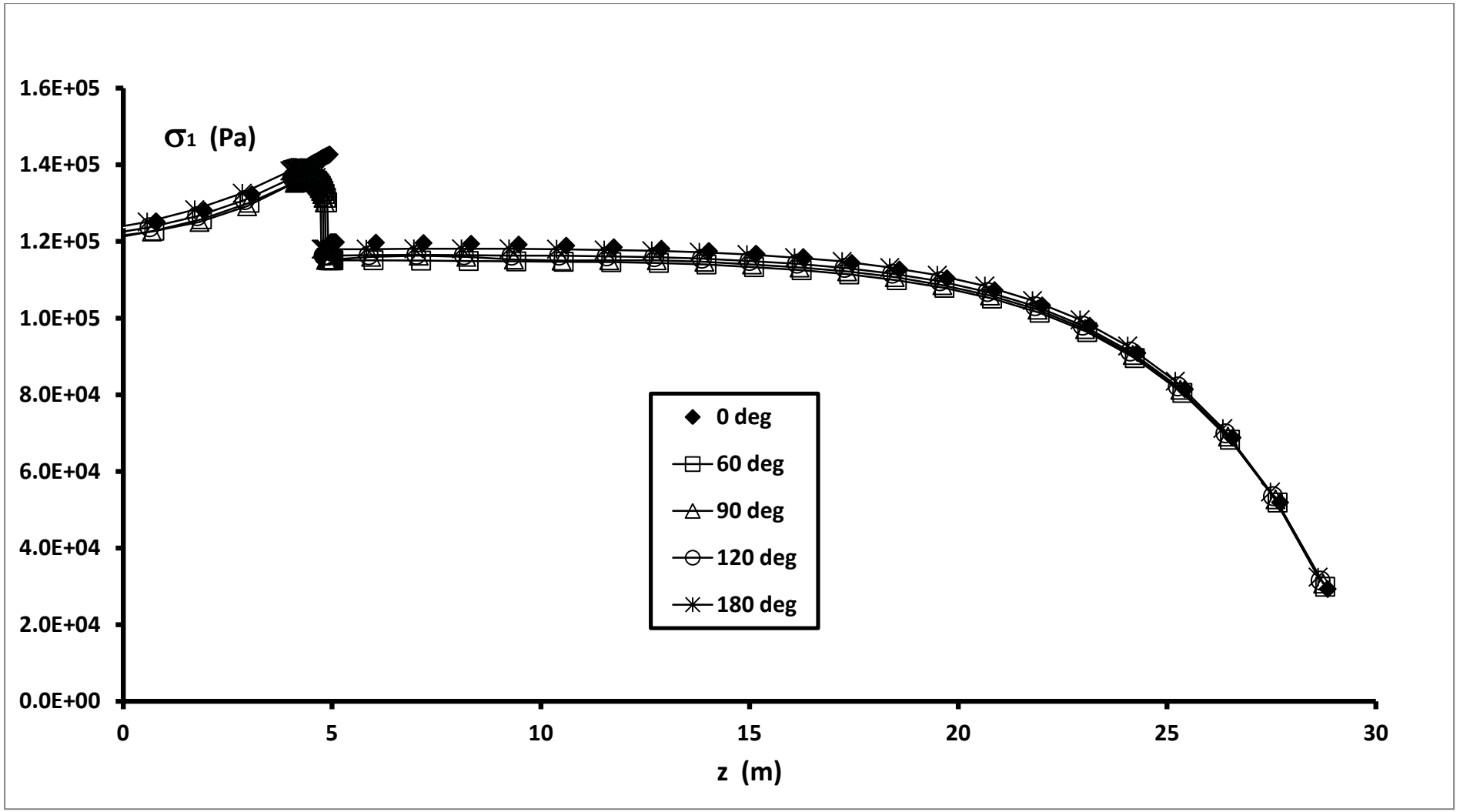

Figure 18 Switch stresses in a silo section 3m radius and 30m tall with an increase in Kw below the switch: conditions shown in Table 5

Figure 18a Principal stress σ_1 versus Cartesian coordinate z

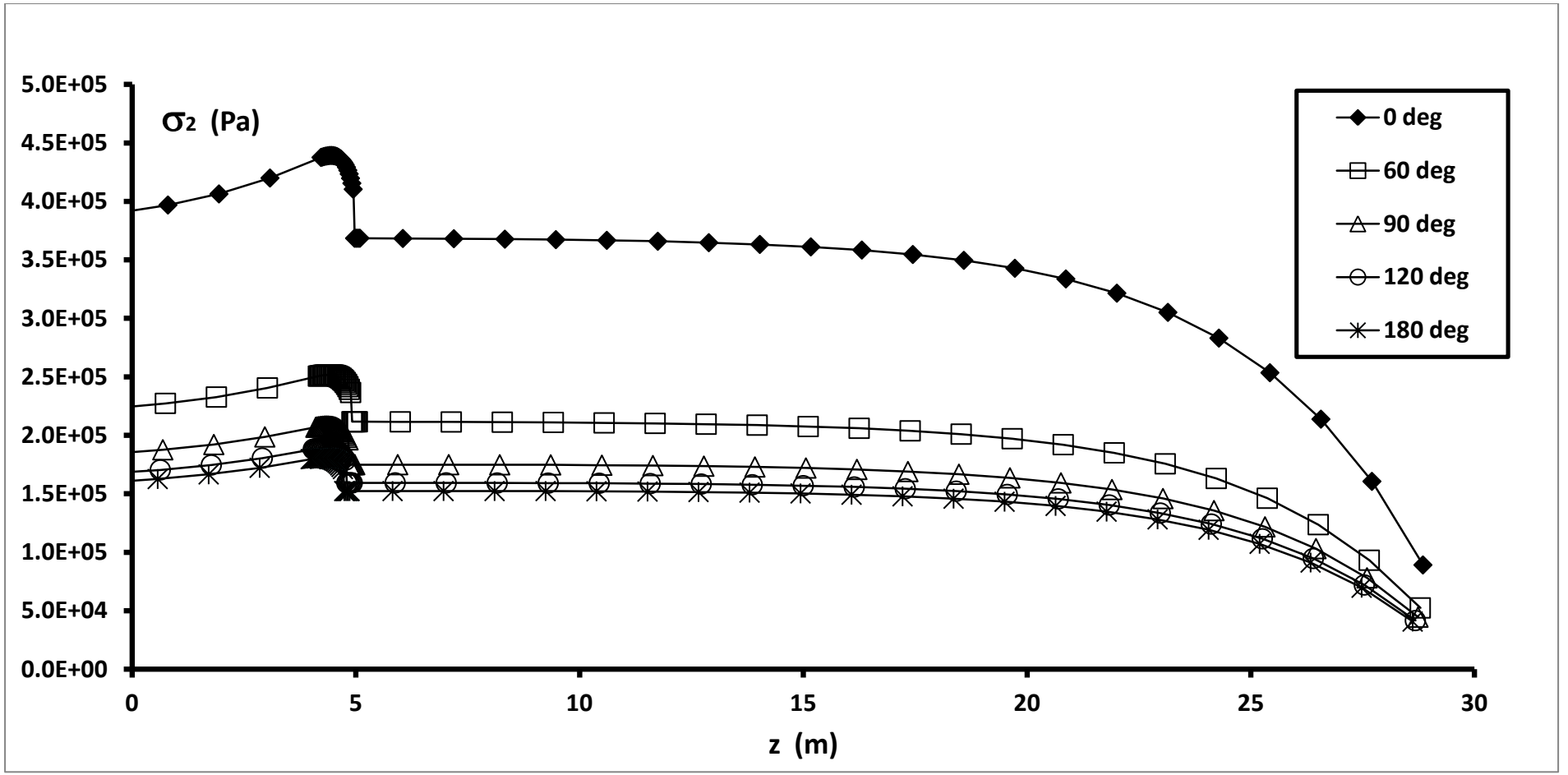

Figure 18 Switch stresses in a silo section 3m radius and 30m tall with an increase in Kw below the switch: conditions shown in Table 5

Figure 18b Principal stress σ_2 versus Cartesian coordinate z

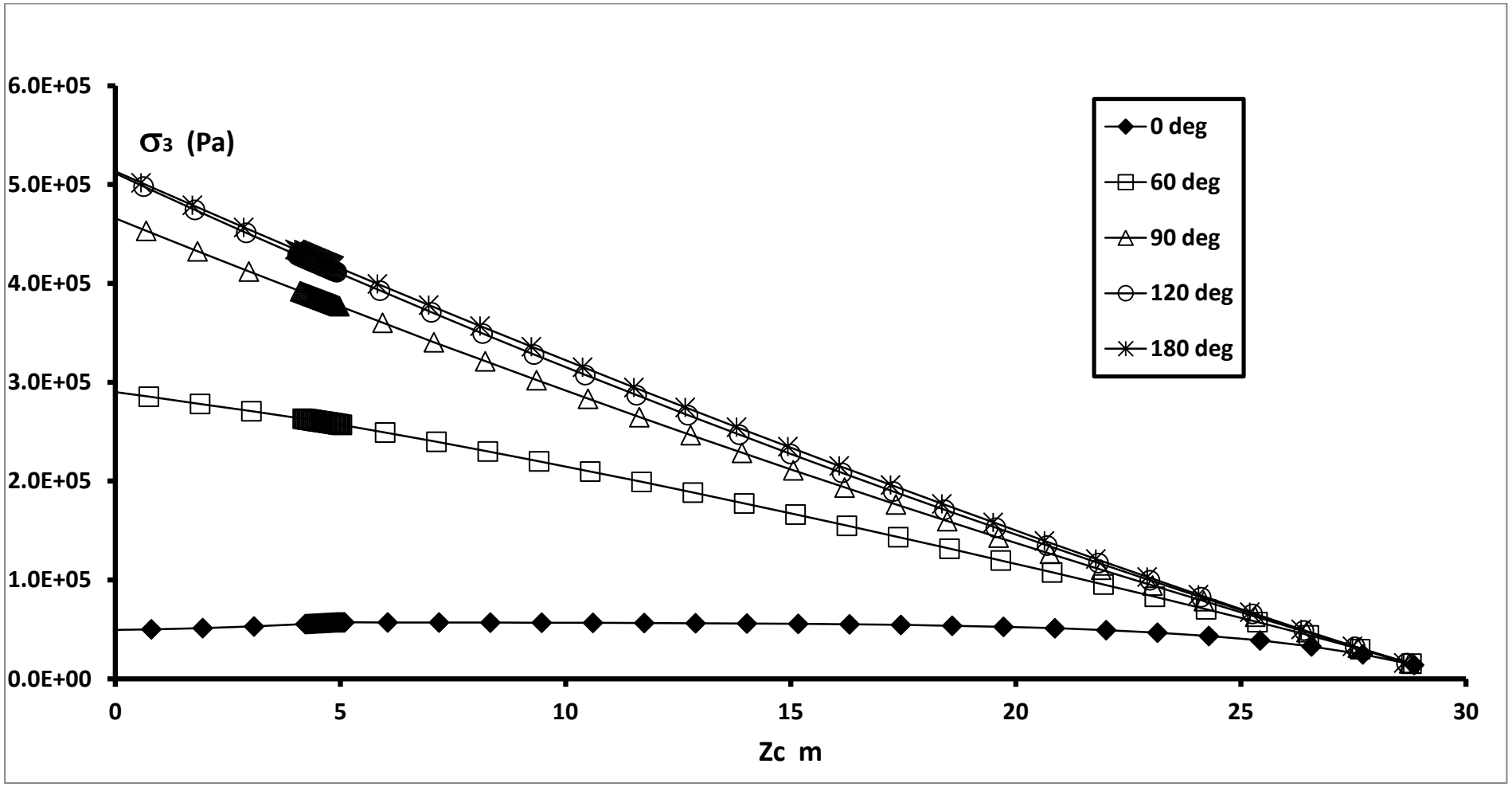

Figure 18 Switch stresses in a silo section 3m radius and 30m tall with an increase in Kw below the switch: conditions shown in Table 5

Figure 18c Principal stress σ_3 versus Cartesian coordinate z

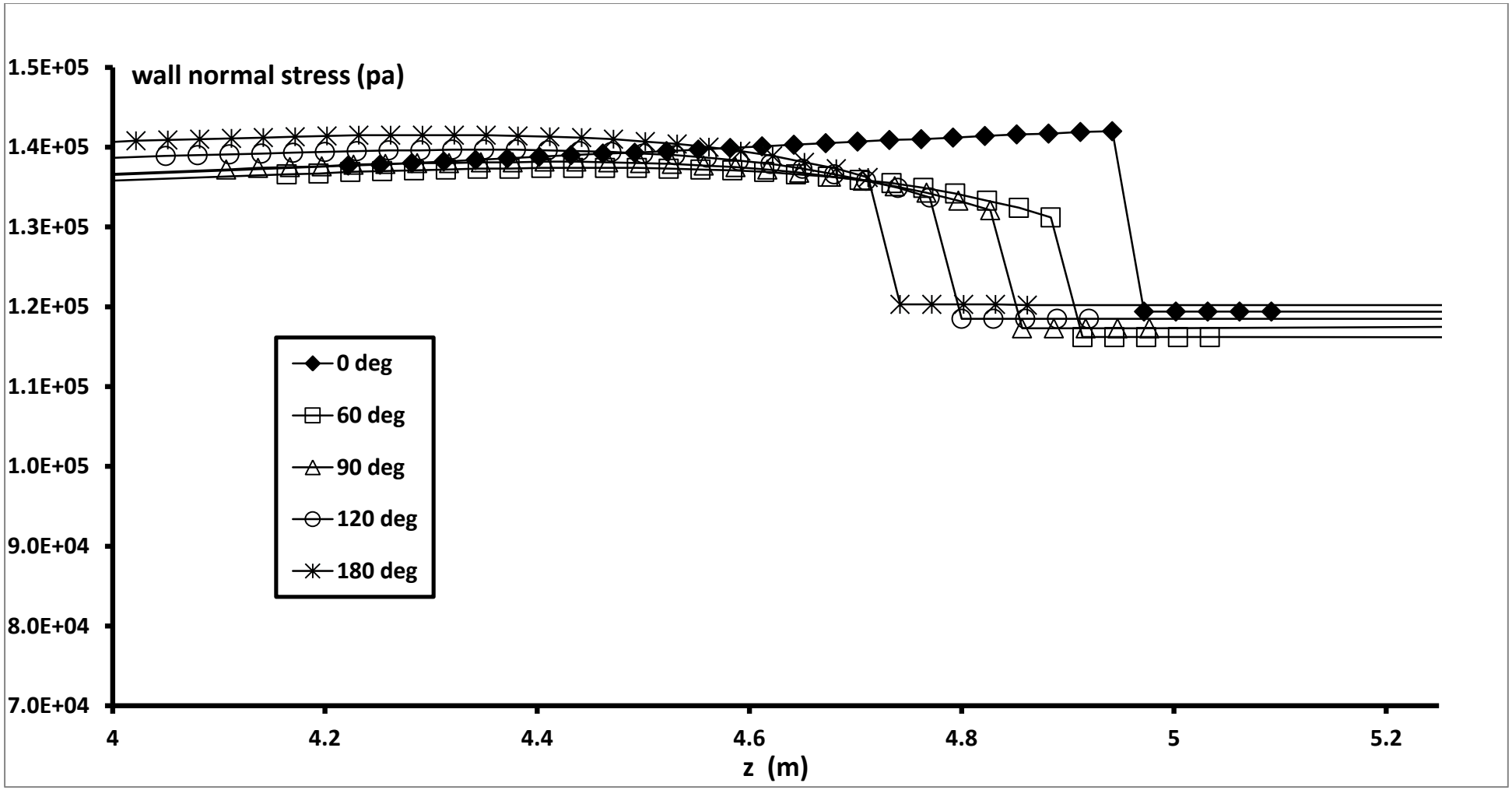

Figure 18 Switch stresses in a silo section 3m radius and 30m tall with an increase in Kw below the switch: conditions shown in Table 5

Figure 18d Wall normal stress in the region of the switch versus Cartesian coordinate z

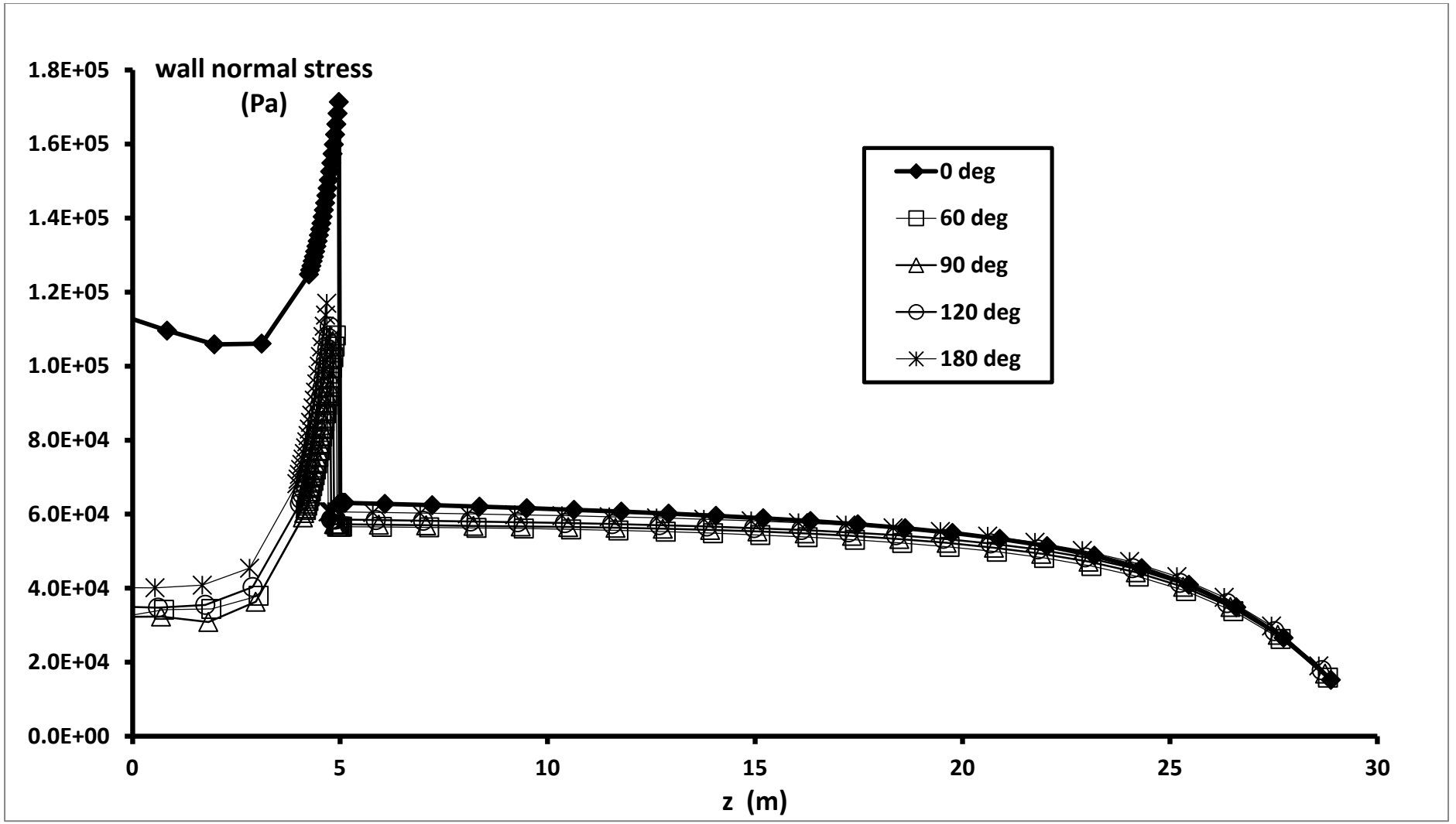

Figure 19 Wall normal stress for conditions close to those of maximum magnitude switch stress. For conditions see Table 5

Figure 19a Overall wall normal stress variation with depth with ε_1 (deg) as a parameter

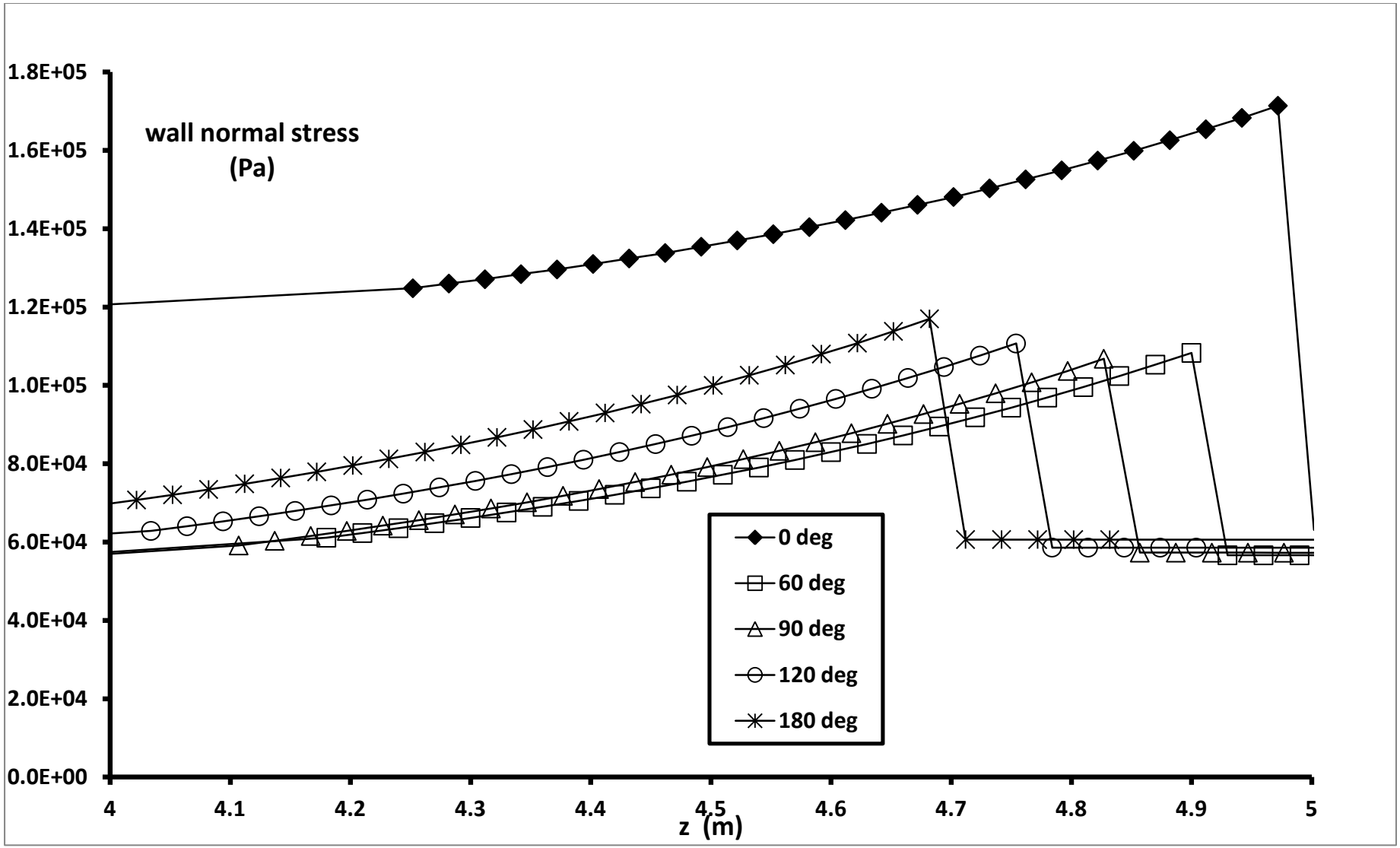

Figure 19 Wall normal stress for conditions close to those of maximum magnitude switch stress. For conditions see Table 5

Figure 19b Wall normal stress in the region of the switch with ε_1 (deg) as a parameter

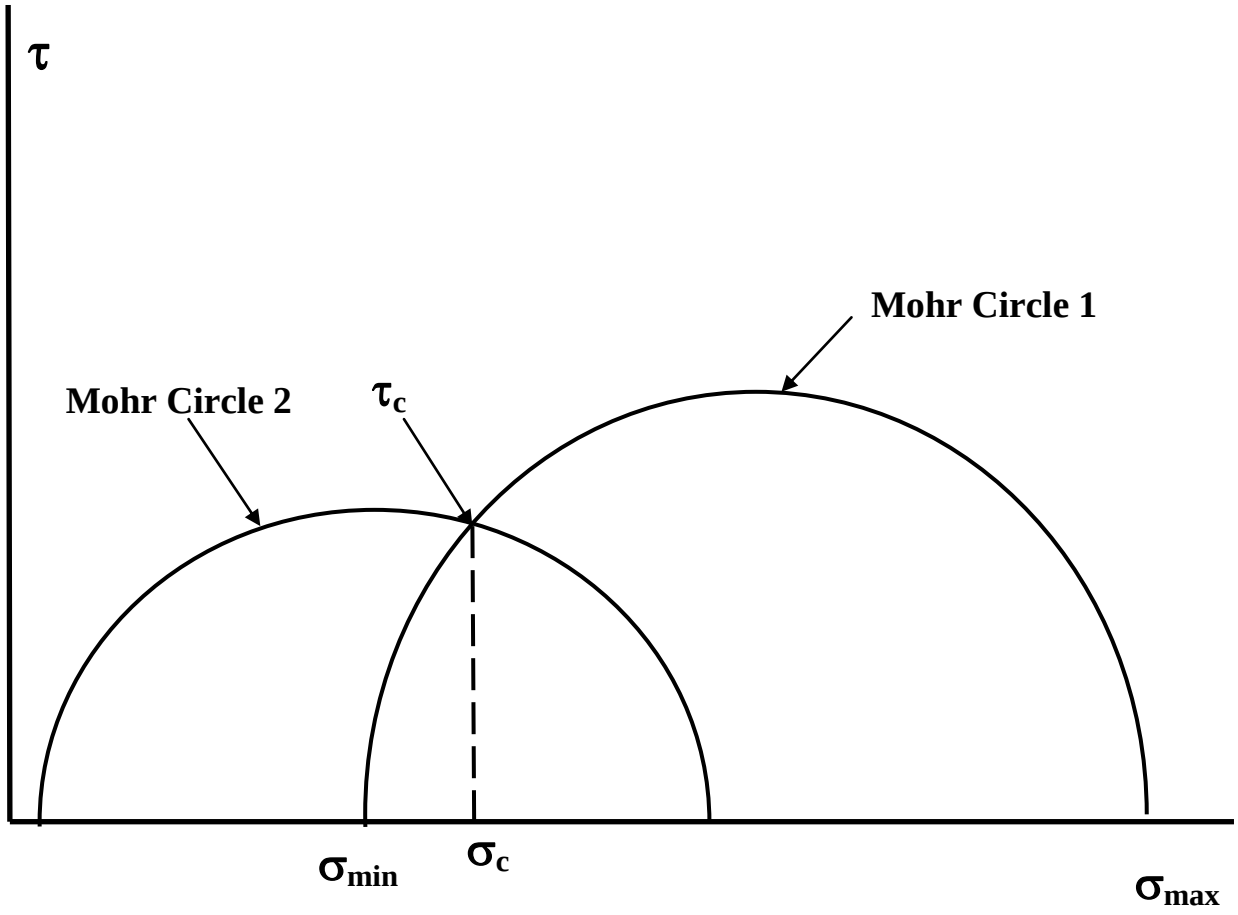

Figure 20 Wall stress measurements - relation to the state of stress, both at the wall and internally